Structural design of a piezoelectric meta-structure with nonlinear electrical Bi-link networks for elastic wave control

Bin Bao, Mickaël Lallart, Daniel Guyomar

Structural design of a piezoelectric meta-structure with nonlinear electrical Bi-link networks for elastic wave control

Bin Bao[a,b*], Mickaël Lallart[a] and Daniel Guyomar[a]

[a]Univ. Lyon, INSA-Lyon, LGEF EA682, F-69621 Villeurbanne, France

[b]Department of Mechanics and Aerospace Engineering, Southern University of Science and Technology, Shenzhen 518055, China

[*]baob@sustech.edu.cn

Abstract

This study reports a structural optimization work of a piezoelectric meta-structure with nonlinear electrical switched Bi-link electronic networks for adaptive wave propagation manipulation and vibration control applications. The investigated meta-structure consists in a periodic arrangement of elementary cells shaping the beam substructure, each of these comprising two piezoelectric elements with connected electrical terminals through semi-passive nonlinear electrical interface, which therefore forms the so-called Bi-link electrical connection. In order to optimize the investigated structure for wave propagation control, the effects of adjusting the geometric/material parameters and locations of the two piezoelectric elements in one periodic cell are analyzed and summarized in detail. Four kinds of structural optimization methods including eighteen structural optimization sub-methods for the open

circuit condition and the SSDI Bi-link condition are concluded and discussed in this research. Results show that the performance of these new resonant-type band gaps can be manipulated to meet the targeted aim in terms of wave propagation characteristics in different frequency domains by proper tuning of the investigated parameters.

Keywords: elastic wave propagation; meta-structure; phononic; synchronized switching damping; piezoelectric.

1. Introduction

In recent years, piezoelectric meta-structures, also called piezoelectric metamaterials [1-5], have attracted a great deal of attention for elastic wave propagation manipulation due to important electromechanical coupling effects [6] on the local resonant bandgap mechanism of mechanical metamaterials [7]. Every periodic cell of piezoelectric meta-structures includes one or several piezoelectric elements for electromechanical energy conversion. Since the effective properties of piezoelectric metamaterials can be precisely customized and tailored through the design of unit electromechanical cells, such meta-structures provide a new way for controlling mechanical waves/vibrations at subwavelength scales in various practical applications such as noise

treatment [8] and structural vibration reduction [9]. For elastic wave propagation investigations, different from purely mechanical metamaterials [10-13] which may be cumbersome to fabricate and integrate physically, smart metamaterials based on smart materials such piezoelectric materials or soft electric materials have the benefit of light add-on mass and easy implementation [14-16]. Furthermore, parameters of smart materials can be tuned through an external electric field without structural modification [17]. For the piezoelectric metamaterials, piezoelectric elements shunted with different kinds of resonant circuits into a unit electromechanical cell can exhibit tunable equivalent damping and/or dynamic stiffness.

In the past few decades, there has been numerous investigations on piezoelectric metamaterials in which piezoelectric elements are shunted with linear resonant circuits [18-21] for manipulating wave propagation. Kherraz *et al.* [22] demonstrated numerically and experimentally the opening of a locally resonant bandgap in a piezoelectric meta-structure made of a homogeneous piezoelectric plate covered by a 1D periodic array of thin electrodes connected to linear inductive shunts. Lee *et al.* [23] studied the effects of the magnitude and phase angle of the resonant shunt impedance on the attenuation constant of a beam with periodic piezoelectric patch arrays so as to determine the optimal shunt that produces the widest and most effective band gaps. Xu *et al.* [24] devised

a piezoelectric metamaterial with linear LC shunt circuits, showing that the bandgap width and depth are significantly enhanced through piezoelectric transducer dimension optimization under a given volume and height of piezoelectric transducers. However, the resonant-type bandgaps of piezoelectric metamaterials with linear resonant shunts are usually narrow in nature, which significantly limits their practical applications under broadband dynamic loads. In order to achieve broadband and controllable resonant-type bandgaps, piezoelectric metamaterials with negative capacitance shunts [25-29] or other active circuit shunts have been developed [30-34].

For the negative capacitance shunts applied to mechanical metamaterials with the plate and beam models, there are many recent researches which demonstrated that the negative capacitance circuit can effectively controll different band gap behaviors in mechanical metamaterials. Chen *et al.* [35] proposed a class of adaptive hybrid metamaterials by integrating negative capacitance shunted piezoelectric patches into a passive locally resonant metamaterial. Results showed that the hybrid metamaterial can be used to "enhance" or "eliminate" (switch ON/OFF) the wave attenuation properties while also allowing the control of the double negative material properties over an extremely broad frequency range. Yu *et al.* [36] investigated the design of piezoelectric metamaterials for broadband vibration control. By shunting identical negative capacitances to the

periodically distributed piezoelectric patches, a wide and continuous band gap is created so as to cover the frequency range of interest.

For the other active circuit shunts applied to mechanical metamaterials, Yi *et al.* [37] proposed a kind of piezoelectric metamaterials with broadband controllable stiffness based on direct active feedback control. The appropriate feedback control law is used for changing the bending stiffness of the active unit, yielding broadened band gaps through the softening or stiffening of the waveguide.

However, these semi-active or active shunts require the use of active electronic circuits that may consume a large amount of energy for the targeted application, and sometimes feature stability issues. In order to overcome these drawbacks, nonlinear electrical circuit techniques have been introduced into piezoelectric metamaterials for wave propagation and vibration control in recent years [38, 39]. Actually, nonlinear electrical circuits have the potential to be designed to realize many different functionalities that have been achieved using nonlinear mechanical metamaterials, such as acoustic rectifier [40], phononic metasurface [41] and phononic transistor [42]. Lallart *et al.* [43] proposed a piezoelectric beam metamaterial with nonlinear electrical networks using independent SSDI (Synchronized Switching Damping on Inductor) shunts. In the investigated periodic cell, each SSDI shunt, which has self-powered versions for implementation [44], is separately connected to

each PZT. Results showed that broadly resonant-type band gaps can be generated by the proposed meta-structure, which are especially suitable for low-frequency multimodal vibration control applications. Zheng *et al.* [45] explored a piezoelectric meta-structure shunted with nonlinear bistable circuits [46] to realize adaptive nonreciprocal wave transmission. However, the factors affecting wave propagation performance of piezoelectric metamaterials with nonlinear electrical networks is not totally comprehensively investigated. Most of the previous studies have focused on investigating the influence of different nonlinear electrical shunts/networks on elastic wave propagation when the investigated piezoelectric meta-structures are already fabricated. Ways of optimizing the structure itself at design stage (structural / material parameters and locations of the piezoelectric elements for instance) to achieve desired wave propagation performance of piezoelectric metamaterials with nonlinear electrical networks are less studied.

In order to release all the potentials of a piezoelectric meta-structure with electrical switched Bi-link electronic networks, a structural optimization research work on the investigated meta-structure is developed for adaptive wave propagation manipulation in this study. The piezoelectric meta-structure with electrical switched Bi-link electronic networks also corresponds to piezoelectric meta-structure with electrical switched 2-order Dual-connected electrical networks which was investigated only

from the electrical aspect [47]. In the periodic cell of the considered architecture, two piezoelectric elements are bonded on the surface of the beam element. The two piezoelectric elements are connected through a SSDI shunt, hence shaping the Bi-link electrical connection. Various factors affecting wave propagation control of the proposed metamaterial are comprehensively analyzed and summarized, including geometric and material parameters as well as the locations of the two piezoelectric elements in one investigated Bi-link periodic cell. Wave propagation performance can be manipulated by parameter adjustment to meet the requirements in terms of wave attenuation performance in different frequency domains before manufacturing.

The article is organized as follows. Section 2 introduces the investigated piezoelectric meta-structure. In Section 3, the wave and finite element modeling approaches for predicting propagative wave performance within the investigated metamaterial is presented. Section 4 aims at analyzing various factors affecting wave propagation control of the investigated metamaterial. Conclusions on the presented work are eventually given in Section 5.

2. Overview of the investigated metamaterial

The investigated metamaterial with electrical switched Bi-link topologies is shown in Figure 1(a). In the Bi-link periodic cell of the investigated metamaterial, two piezoelectric elements are connected by a SSDI shunt. Herein, PZT is used to refer to the piezoelectric element. All the PZTs attached on the beam substructure are assumed identical and equidistant in the standard version of the investigated piezoelectric metamaterial. In order to investigate and compare different effects of PZT parameters and locations on wave propagation properties, the standard version of the investigated piezoelectric metamaterial is considered as a reference structure for performance comparison at the following sections. Accordingly, the reference Bi-link periodic cell is as shown in Figure 1(b). According to different adjustment methods of PZT parameters and locations on wave propagation properties, the Bi-link periodic cell can be divided into four kinds: (1) Bi-link periodic cell with adjustable spacing between two PZTs as shown in Figure 1(b1); (2) Bi-link periodic cell with adjustable lengths of two PZTs as shown in Figure 1(b2); (3) Bi-link periodic cell with adjustable thicknesses of two PZTs as shown in Figure 1(b3); (4) Bi-link periodic cell with adjustable charge coefficients of two PZTs as shown in Figure 1(b4).

The electrical interface of the investigated piezoelectric meta-structure consists in the nonlinear SSDI techniques, where the piezoelectric voltage or voltage difference is quickly inverted at each occurrence of displacement or displacement difference extremum of the structure, yielding a voltage magnification through a cumulative process as well as a decrease of the time shift between voltage and velocity, both of these effects denoting an increase of the mechanical energy irreversibly converted into electrical energy (which in turns significantly reduces the mechanical energy implying damping effect).

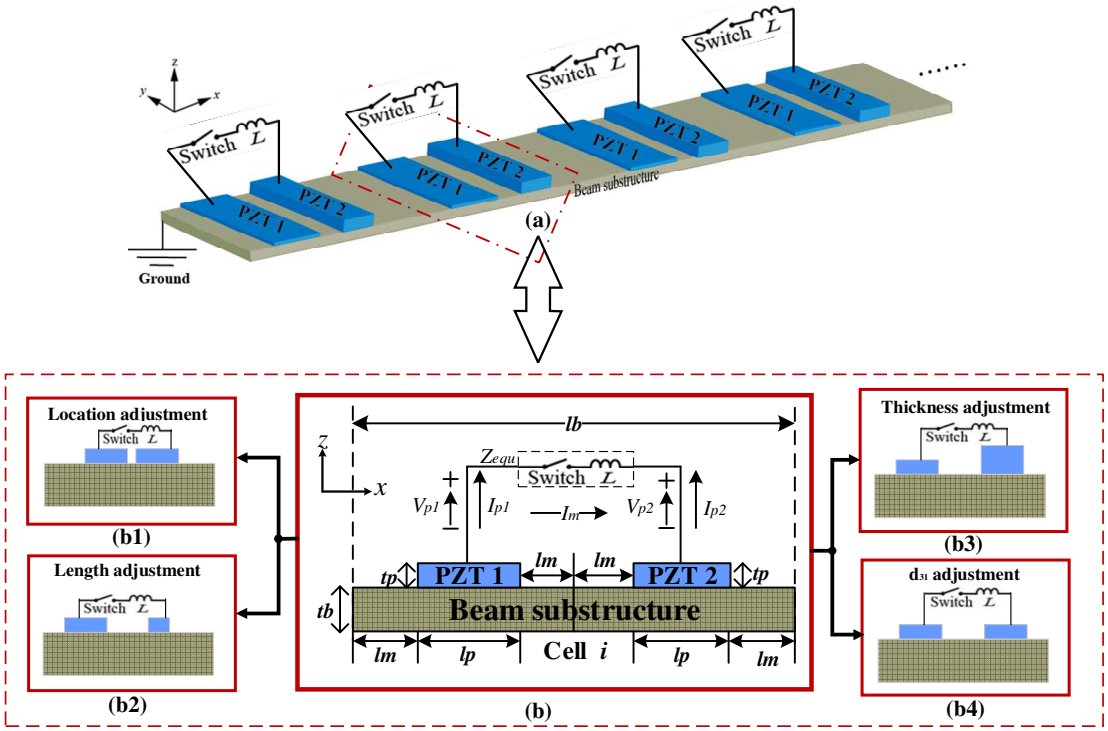

Figure 1 (a) Piezoelectric metamaterial with electrical switched Bi-link topologies; (b) one reference Bi-link periodic cell with detailed descriptions; (b1) one Bi-link periodic cell with changeable PZT

locations; (b2) one Bi-link periodic cell with adjustable PZT lengths; (b3) one Bi-link periodic cell with adjustable PZT thicknesses; (b4) Bi-link periodic cell with different PZT charge coefficients.

A SSDI control shunt consisting of an electronic switch in series with an inductor is applied between two PZTs bonded on the piezoelectric structure, as shown in Figure 2. When the PZT is in the open circuit condition, the piezoelectric voltage varies with the piezoelectric strain in a linear fashion. When an extremal voltage difference between two PZTs appears, the switch is closed, and then an oscillator is formed. The oscillator is made of the inductance L and the equivalent capacitance C_e of the two PZTs. The switching time period is equal to half of the pseudo-period of this oscillator. For most of the time in one mechanical vibration period, the switch is open. The technique is besides adaptive to frequency shifts due to the extremum detection principles.

During the closed time of the switch, the voltage between both ends of the switch interface is inverted imperfectly, since the switching network (electronic switch + inductance) dissipates a portion of the energy stored on the inherent capacitance of the piezoelectric element. Such energy losses can be characterized by an electrical quality factor Q_e, as follows:

$$Q_e = \frac{1}{r}\sqrt{\frac{L}{C_e}} \tag{1}$$

Where r denotes the total equivalent resistance of the switching network. The relationship between the equivalent factor Q_e and the voltage difference of two PZTs before (V_{Md}) and after (V_{md}) the inversion process can also be given by:

$$\gamma_{diff} = \frac{V_{md}}{V_{Md}} = e^{-\frac{\pi}{2Q_e}} \tag{2}$$

where γ_{diff} denotes the inversion coefficient of the voltage difference between two PZTs.

According to the literatures [9, 48, 49], the SSDI equivalent (linearized) impedance Z_e between two PZTs can be estimated by using first harmonic approximation in the frequency domain, yielding：

$$Z_e = \frac{\pi\left(1-\gamma_{diff}\right)}{4\omega C_e\left(1+\gamma_{diff}\right)} + j\frac{1}{\omega C_e}, C_e = \frac{C_1 C_2}{C_1 + C_2} \tag{3}$$

Where C_1 and C_2 respectively refer to the clamped capacitance of two PZTs in the Bi-link connection. ω is the angular frequency.

As described by the above equation, the imaginary part of the nonlinear SSDI impedances matches the optimized imaginary part of the electronic load in linear Bi-link approach, denoting the SSDI capability of automatic impedance adaptation. Through the calculation of the equivalent damping ratio, it can be found that the resonant SSDI control system is stable and underdamped, and will always resonate when driven by an external oscillation. Therefore, high system stability can be achieved for modifying the physical properties of a smart vibration control system

through the use of electrical SSDI impedance connected across the electrodes of PZTs.

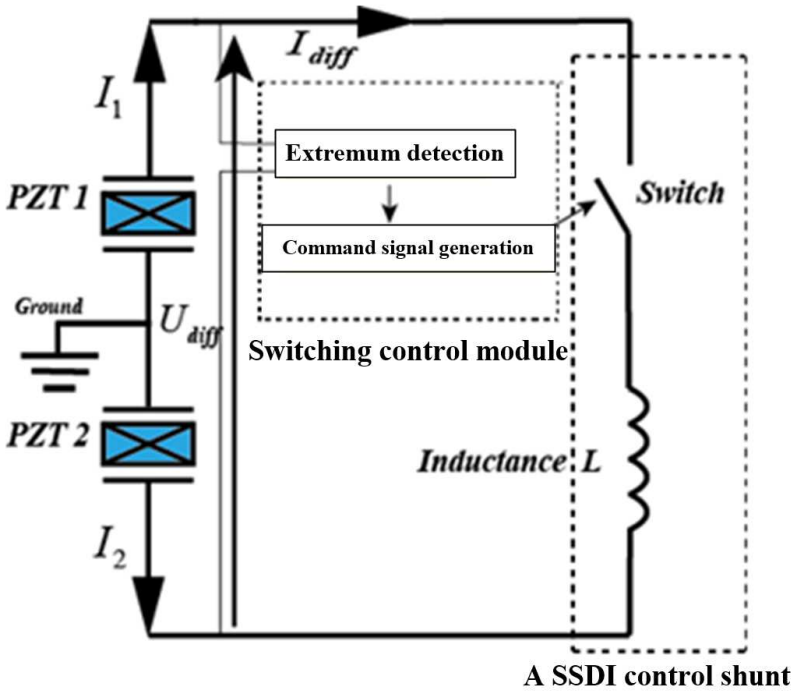

Figure 2 schematic diagram of a SSDI control shunt connected between two identical PZTs in which the switch signal is generated by the switching control module for a SSDI control shunt to switch the piezoelectric voltage difference between two PZTs.

3. Modeling of the investigated piezoelectric meta-structure

According to the finite element modeling (FEM) method of a Euler-Bernoulli piezoelectric beam and considering that the Bi-link periodic cell in the investigated piezoelectric meta-structure can be divided into *n* finite elements in the frequency domain[47] as shown in

Figure 3, the fundamental electromechanical relationships within the cell i ($i \in [1,m]$, m being the total number of cells) can be given by:

$$\begin{cases} \left[-\omega^2 M_{unit}\right]\left\{d^i\right\} + \left[j\omega C_{unit}\right]\left\{d^i\right\} + \left[K_{unit}\right]\left\{d^i\right\} + \left[B_1^e\right]\left\{V_p{}^i\right\} = \left\{P^i\right\} \\ \left\{I_p{}^i\right\} = \left[j\omega B_2^e\right]\left\{d^i\right\} + \left[j\omega B_3^e\right]\left\{V_p{}^i\right\} \end{cases} \tag{4}$$

$$\left[M_{unit}\right] = \int_0^l [H]^T \rho A [H] dx, \quad \left[K_{unit}\right] = \int_0^l [H'']^T EI [H''] dx, \quad \left[C_{unit}\right] = \beta_1 \left[M_{unit}\right] + \beta_2 \left[K_{unit}\right]$$

where the mass matrices, Rayleigh damping matrices and short-circuit stiffness matrices are respectively denoted as M_{unit}, C_{unit}, K_{unit}. The length of finite beam element is denoted as l. The matrix of Hermitian shape function and the second order derivative of Hermitian shape functions are respectively denoted as H and H''. The mass density of the material is denoted as ρ, The cross-sectional area of the beam is denoted as A, The elastic modulus of the beam is denoted as E, and the second moment of the cross-sectional area of the beam is denoted as I. The damping coefficient constants following Rayleigh damping assumption are β_1 and β_2. the generalized nodal displacement vectors (displacement and slope vectors in the frequency domain) and the generalized nodal force vectors (force and moment vectors in the frequency domain) are respectively represented as d^i and P^i (2(n+1) by 1 matrices). The piezoelectric voltages and output currents of identical piezoelectric elements in the investigated periodic cell are respectively denoted as $\{V_p{}^i\}$ and $\{I_p{}^i\}$, and their matrix size is determined by the number of piezoelectric elements in the unit investigated periodic cell. The electromechanical matrix $B_1{}^e$ (2(n+1) by 2)

and the electromechanical matrix B_2^e (2 by 2(n+1)) can be given as:

$$B_1^e = \begin{bmatrix} B_{11} & B_{12} \end{bmatrix}, \begin{cases} B_{11} = b_{11}\int_0^l [H'']^T dx, b_{11} = -\dfrac{p_1 d_{31}^{p1} w_b}{t_{p1}\left(s_{11}^{Ep1} + s_{12}^{Ep1}\right)} \int_{t_b}^{t_b+t_{p1}} (u_3 - x_c)\, dx_3 \\ B_{12} = b_{12}\int_0^l [H'']^T dx, b_{12} = -\dfrac{p_2 d_{31}^{p2} w_b}{t_{p2}\left(s_{11}^{Ep2} + s_{12}^{Ep2}\right)} \int_{t_b}^{t_b+t_{p2}} (u_3 - x_c)\, dx_3 \end{cases} \tag{5}$$

$$B_2^e = \begin{bmatrix} B_{21} \\ B_{22} \end{bmatrix}, \begin{cases} B_{21} = b_{21}\int_0^l [H'']dx,\ b_{21} = -\dfrac{p_1 d_{31}^{p1} t_{p1}}{\left(s_{11}^{Ep1} + s_{12}^{Ep1}\right)} \\ B_{22} = b_{22}\int_0^l [H'']dx,\ b_{22} = -\dfrac{p_2 d_{31}^{p2} t_{p2}}{\left(s_{11}^{Ep2} + s_{12}^{Ep2}\right)} \end{cases} \tag{6}$$

where the signs of piezoelectric constant p_1, p_2 depend on the polarization direction of the PZTs (1, 2): when the direction is positive, it is assumed equal to 1, and when negative, it is assumed equal to -1.

The matrix B_3^e is a 2 by 2 electrical (capacitance) matrix whose expression yields:

$$B_3^e = \begin{bmatrix} B_{31} & 0 \\ 0 & B_{32} \end{bmatrix}, \begin{cases} B_{31} = \dfrac{w_b l_{p1}\left[2\left(d_{31}^{p1}\right)^2 - \varepsilon_{33}^T\left(s_{11}^{Ep1} + s_{12}^{Ep1}\right)\right]}{t_{p1}\left(s_{11}^{Ep1} + s_{12}^{Ep1}\right)} \\ B_{32} = \dfrac{w_b l_{p2}\left[2\left(d_{31}^{p2}\right)^2 - \varepsilon_{33}^T\left(s_{11}^{Ep2} + s_{12}^{Ep2}\right)\right]}{t_{p2}\left(s_{11}^{Ep2} + s_{12}^{Ep2}\right)} \end{cases} \tag{7}$$

Denoting the dynamical stiffness matrix of the short-circuited system [A^e], that is equal to:

$$\left[A^e\right] = \left[-\omega^2 M_{unit}\right] + \left[j\omega C_{unit}\right] + \left[K_{unit}\right] \tag{8}$$

The Bi-link periodic cell in different cases as shown in Figure 1(b, b1, b2, b3, b4) holds the same relationships:

$$P^i = A^e d^i + B_1^e V_p^i \tag{9}$$

$$I_p^i = \begin{bmatrix} I_{p1} \\ I_{p2} \end{bmatrix}, V_p^i = \begin{bmatrix} V_{p1} \\ V_{p2} \end{bmatrix} \tag{10}$$

$$I_{p1} = B_{21}\dot{d}^i + B_{31}\dot{V}_{p1} \tag{11}$$

$$I_{p2} = B_{22}\dot{d}^i + B_{32}\dot{V}_{p2} \tag{12}$$

$$I_{p1} = I_m, I_{p2} = -I_m \tag{13}$$

$$V_{p1} - I_m Z_e = V_{p2} \tag{14}$$

$$Z_e = \frac{\pi\left(1-\gamma_{diff}\right)}{4\omega C_e\left(1+\gamma_{diff}\right)} + j\frac{1}{\omega C_e} \tag{15}$$

Therefore, the voltages V_{p1}, V_{p2} , $V_p{}^i$ can be obtained as:

$$V_{p1} = \left[-\frac{j\omega B_{21} + j\omega B_{22} + \omega^2 B_{21}B_{32}Z_e}{j\omega B_{31} + j\omega B_{32} + \omega^2 B_{31}B_{32}Z_e} \right] d^i \tag{16}$$

$$V_{p2} = \left[\left(j\omega B_{31}Z_e - 1\right) \frac{j\omega B_{21} + j\omega B_{22} + \omega^2 B_{21}B_{32}Z_e}{j\omega B_{31} + j\omega B_{32} + \omega^2 B_{31}B_{32}Z_e} - j\omega B_{21}Z_e \right] d^i \tag{17}$$

$$V_p^i = B_6^e d^i, B_6^e = \begin{bmatrix} -\dfrac{j\omega B_{21} + j\omega B_{22} + \omega^2 B_{21}B_{32}Z_e}{j\omega B_{31} + j\omega B_{32} + \omega^2 B_{31}B_{32}Z_e} \\ \left[\left(j\omega B_{31}Z_e - 1\right) \dfrac{j\omega B_{21} + j\omega B_{22} + \omega^2 B_{21}B_{32}Z_e}{j\omega B_{31} + j\omega B_{32} + \omega^2 B_{31}B_{32}Z_e} - j\omega B_{21}Z_e \right] \end{bmatrix} \tag{18}$$

The relationships of the reference Bi-link periodic cell as shown in Figure 1(b) yield:

$$\begin{cases} p_1 = p_2 = 1, \quad t_{p1} = t_{p2} = t_p, \quad d_{31}^{p1} = d_{31}^{p2} = d_{31} \\ s_{11}^{Ep1} = s_{11}^{Ep2}, \quad s_{12}^{Ep1} = s_{12}^{Ep2}, \quad l_{p1} = l_{p2} = l_p \end{cases} \tag{19}$$

For simplification, the voltages $V_p{}^i$ can be simplified as:

$$V_p^i = B_6^e d^i, B_6^e = \begin{bmatrix} \dfrac{-\dfrac{2B_{21}}{B_{31}} + j\omega Z_e B_{21}}{2 - j\omega Z_e B_{31}} \\ -\dfrac{2B_{21}}{B_{31}} - \dfrac{-\dfrac{2B_{21}}{B_{31}} + j\omega Z_e B_{21}}{2 - j\omega Z_e B_{31}} \end{bmatrix} \tag{20}$$

Finally, the dynamical relationships of the SSDI Bi-link periodic cell can be given by:

$$\left\{P^i\right\} = A^e_{\text{Bi-link}} \cdot d^i = \left(A^e + B^e_1 B^e_6\right) \cdot d^i \tag{21}$$

In order to clearly present the electro-mechanical coupling of the proposed structure, the equations (13) and (18) are introduced in detail in the equation (19), Therefore, the dynamical relationships of the SSDI Bi-link periodic cell can also be given by:

$$\left\{P^i\right\} = \left(\left[-\omega^2 M_{unit}\right] + \left[j\omega C_{unit}\right] + \left[K_{unit}\right] + \left[B_{11} \quad B_{12}\right] \begin{bmatrix} \dfrac{-\dfrac{2B_{21}}{B_{31}} + j\omega B_{21}\left(\dfrac{\pi\left(1-\gamma_{diff}\right)}{4\omega C_e\left(1+\gamma_{diff}\right)} + j\dfrac{1}{\omega C_e}\right)}{2 - j\omega B_{31}\left(\dfrac{\pi\left(1-\gamma_{diff}\right)}{4\omega C_e\left(1+\gamma_{diff}\right)} + j\dfrac{1}{\omega C_e}\right)} \\ -\dfrac{2B_{21}}{B_{31}} - \dfrac{-\dfrac{2B_{21}}{B_{31}} + j\omega B_{21}\left(\dfrac{\pi\left(1-\gamma_{diff}\right)}{4\omega C_e\left(1+\gamma_{diff}\right)} + j\dfrac{1}{\omega C_e}\right)}{2 - j\omega B_{31}\left(\dfrac{\pi\left(1-\gamma_{diff}\right)}{4\omega C_e\left(1+\gamma_{diff}\right)} + j\dfrac{1}{\omega C_e}\right)} \end{bmatrix} \right) \cdot d^i \tag{22}$$

As shown in the equation (22), the dynamical relationships of the SSDI periodic cell can be greatly affected by the electrical parameters of the nonlinear SSDI circuits such as the voltage inversion coefficient γ_{diff} and the equivalent capacitance C_e of the two PZTs. The influences of the SSDI electrical parameters on such structure was discussed in detail in the literature [47]. While this research focuses on the structural design and optimization of such structure with nonlinear electrical networks.

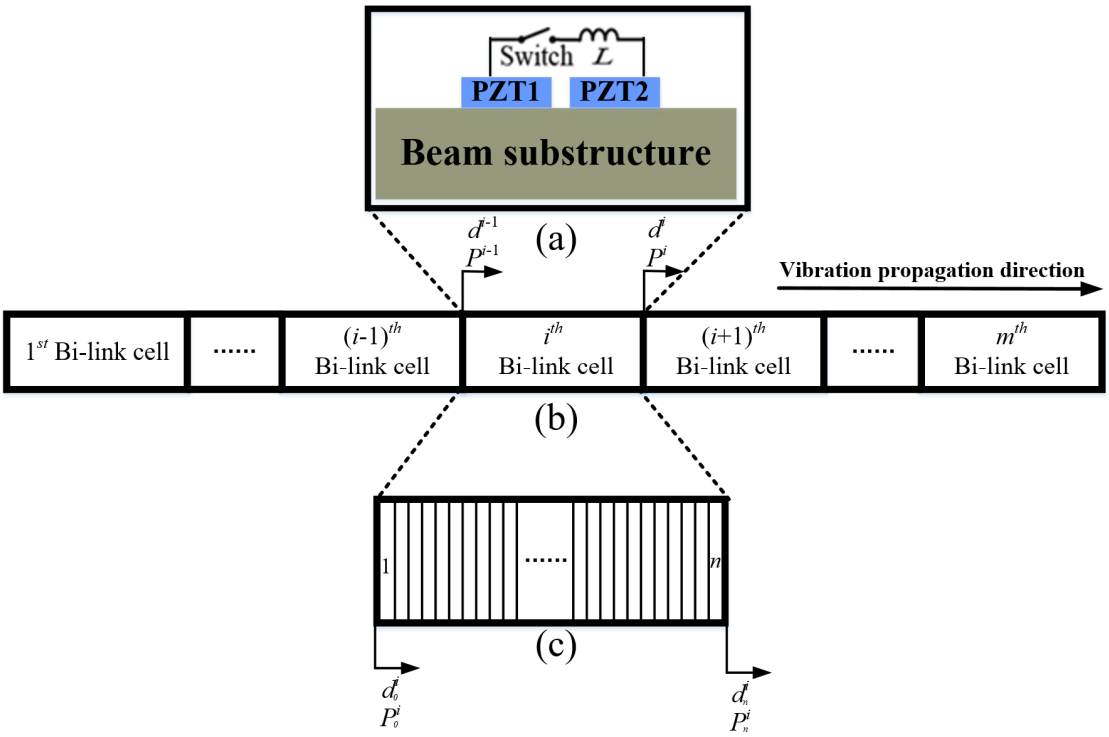

Figure 3 (a) the investigated Bi-link periodic cell; (b) the piezoelectric metamaterial composed of the investigated Bi-link periodic cells； (c) the finite element decomposition of the Bi-link periodic cell.

4. Numerical result analysis

4.1 Wave propagation performance of the initial reference metamaterial with identical PZTs and spacing

Wave attenuation characteristics of the investigated piezoelectric meta-structure are theoretically compared and discussed in this section based on a sample whose parameters are listed in Table 1 and Table 2. The reference Bi-link periodic cell includes two identical PZTs bonded symmetrically on the beam substructure, as shown in Figure 1(b). Wave

attenuation performance of the metamaterial composed of reference Bi-link periodic cells is considered as a reference object or an initial metamaterial for investigating and comparing the effects of different structural parameters on wave attenuation performance of the investigated metamaterial. “Reference SSDI Bi-link” in all the following figures denotes wave attenuation performance of the investigated metamaterial composed of reference Bi-link periodic cells. Specifically, the dimension of a reference Bi-link periodic cell is 44 mm. Each PZT is 10 mm long. The detailed geometric parameters of the Bi-link periodic cell are given as:

$$\begin{cases} l_{p1} = l_{p2} = l_p, \quad l_p = 10\text{mm}, \quad l_m = 6\text{mm} \\ t_{p1} = t_{p2} = t_p, \quad t_p = 0.5\text{mm}, \quad t_b = 1.5\text{mm} \\ l_b = 4l_m + 2l_p = 44\text{mm} \end{cases} \tag{23}$$

Table 1 Dimensional and material properties of the beam substructure

Young modulus	Y_b=190×10 ^{9}Pa	Poisson ratio	v_b=0.21	Beam density	ρ_b=7875 kg/m^3
Beam length	L_b=176mm	Beam width	w_b=35mm	Beam thickness	t_b=1.5mm

Table 2 Dimensional and material properties of the PZT

Short-circuit Compliance	s_{11}^E=10.7×10^{-12}m^2/N s_{12}^E=−3.3×10^{-12}m^2/N	PZT length	l_p=10mm
Charge coefficient	d_{31}=−108×10^{-12}m/V	PZT thickness	t_p=0.5mm
Relative dielectric constant	$\varepsilon^T/\varepsilon_0$=1150	PZT density	ρ_p=7650 kg/m^3

The investigated Bi-link periodic cell is decomposed into several finite beam elements according to Finite Element Modeling analysis as shown in Figure 3. Propagation coefficients representing wave attenuation properties of mechanical metamaterials include attenuation coefficient and phase coefficient. Herein, we mainly focus on attenuation coefficient in the framework of vibration reduction purposes. Attenuation coefficient denotes the logarithmic decay of the vibration amplitude of an elastic wave propagating from one periodic cell to the next one. In order to obtain attenuation coefficient under different electrical boundary conditions, transfer matrix for the whole cell is derived using transfer matrix method [9]. Herein, only positive direction is taken into account in the following analysis and no structural damping ($[\boldsymbol{C}_{unit}]$= [0]) is considered.

According to the vibration propagation direction as shown in Figure 3, the following relationships exist:

$$\begin{cases} d^{i-1} = d_n^{i-1} = d_0^i; \\ P^{i-1} = P_n^{i-1} = -P_0^i; \\ d^i = d_n^i = d_0^{i+1}; \\ P^i = P_n^i = -P_0^{i+1} \end{cases} \tag{24}$$

The form of Eq.(21) can be rearranged by separation of extreme vectors from internal vectors of one Bi-link periodic cell:

$$\begin{Bmatrix} P_0^i \\ P_j^i \\ P_n^i \end{Bmatrix} = \left[A_{Bi-link}^e \right] \cdot \begin{Bmatrix} d_0^i \\ d_j^i \\ d_n^i \end{Bmatrix} = \begin{bmatrix} a_{00} & a_{0j} & a_{0n} \\ a_{j0} & a_{jj} & a_{jn} \\ a_{n0} & a_{nj} & a_{nn} \end{bmatrix} \cdot \begin{Bmatrix} d_0^i \\ d_j^i \\ d_n^i \end{Bmatrix} \tag{25}$$

According to Guyan's reduction, expressions of the dynamic response of one electromechanical periodic cell without external load can be simplified as:

$$\begin{Bmatrix} P_0^i \\ P_n^i \end{Bmatrix} = \begin{bmatrix} \underbrace{a_{00} - a_{0j} a_{jj}^{-1} a_{j0}}_{\alpha_{11}} & \underbrace{a_{0n} - a_{0j} a_{jj}^{-1} a_{jn}}_{\alpha_{12}} \\ \underbrace{a_{n0} - a_{nj} a_{jj}^{-1} a_{j0}}_{\alpha_{21}} & \underbrace{a_{nn} - a_{nj} a_{jj}^{-1} a_{jn}}_{\alpha_{22}} \end{bmatrix} \cdot \begin{Bmatrix} d_0^i \\ d_n^i \end{Bmatrix} \tag{26}$$

Therefore, the transfer matrix T of the Bi-link periodic cell can be written as,

$$\begin{Bmatrix} d_n^i \\ P_n^i \end{Bmatrix} = T \cdot \begin{Bmatrix} d_0^i \\ P_0^i \end{Bmatrix} = \begin{bmatrix} -\alpha_{12}^{-1}\alpha_{11} & \alpha_{12}^{-1} \\ -\alpha_{21} + \alpha_{22}\alpha_{12}^{-1}\alpha_{11} & -\alpha_{22}\alpha_{12}^{-1} \end{bmatrix} \cdot \begin{Bmatrix} d_0^i \\ P_0^i \end{Bmatrix} \tag{27}$$

And then, the propagation coefficients are obtained with the calculation of eigenvalues $eig\left(T\right)_i \left(i = 1,2,3,4\right)$ of the transfer matrix T:

$$eig\left(T\right)_i = e^{jk_i L} = e^{\mu} = e^{\alpha + j\phi} \tag{28}$$

Where k_i is the complex wavenumber, L is the length of a periodic cell, μ is a complex number, α denotes the logarithmic decay of the vibration amplitude of a wave propagating from one cell to the next one, namely the attenuation coefficient, and ϕ represents the phase difference between the wave in two adjacent cells, called 'phase coefficient'.

Figure 4(a) shows wave attenuation performance of the reference metamaterial including reference Bi-link periodic cells with identical PZTs and spacing in the open circuit condition. It can be seen that two generated Bragg-type band gaps respectively appear in the frequency ranges [7.2 kHz, 8.1 kHz] ∪ [29 kHz, 32 kHz]. Figure 4(b) shows wave attenuation performance of the metamaterial including reference SSDI Bi-link periodic cells when the voltage inversion coefficient γ_{diff} is equal to 0.6. Compared to the open circuit condition, the SSDI Bi-link case exhibits better attenuation performance in the frequency ranges [0 kHz, 29 kHz] ∪ [32 kHz, 35 kHz]. It should be noted that the rationality and correctness of wave attenuation performance of the initial metamaterial including reference Bi-link periodic cells with identical PZTs were previously demonstrated in the literature [47]. The main work of this research is the structural design for the piezoelectric meta-structure with electrical switched Bi-link electronic networks for adaptive wave propagation manipulation.

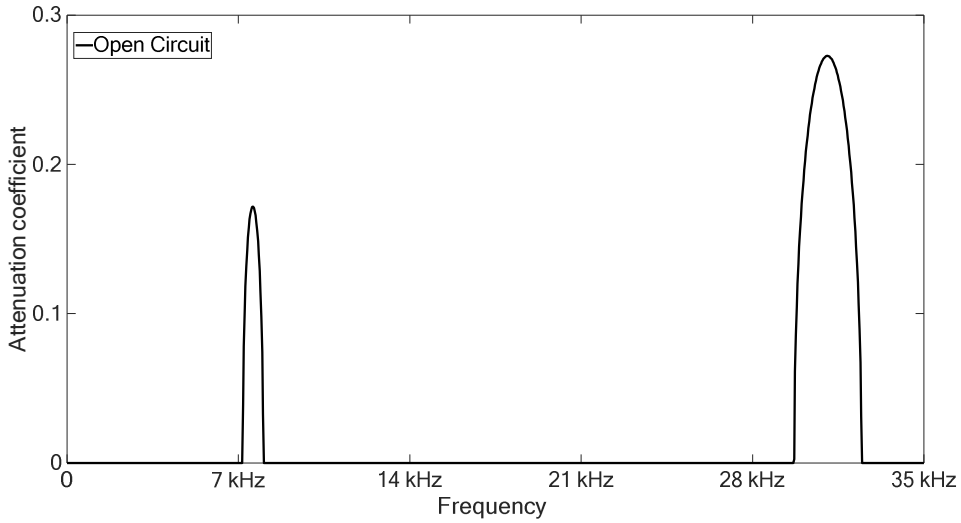

(a)

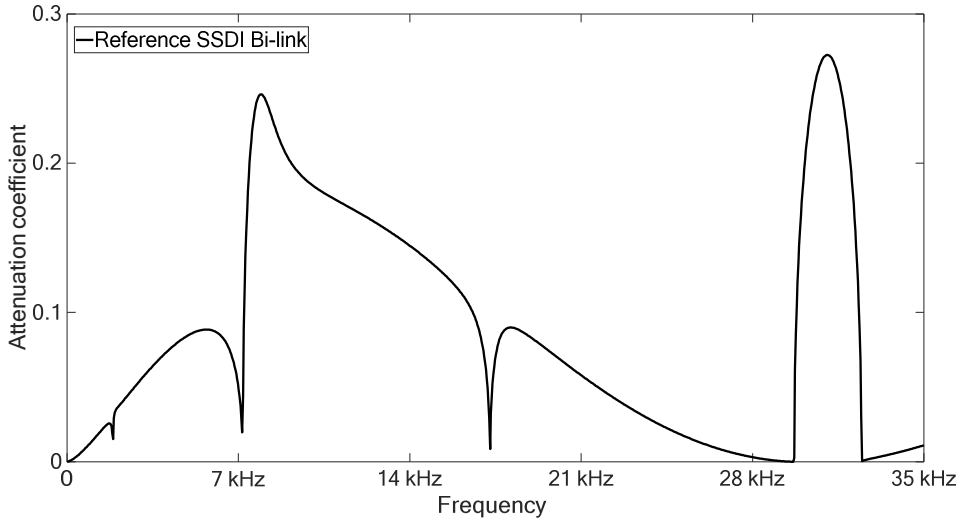

(b)

Figure 4 (a) Wave attenuation performance of the metamaterial including reference Bi-link periodic cells with identical PZTs and spacing in the open circuit condition; (b) wave attenuation performance of the initial metamaterial including reference SSDI Bi-link periodic cells. The frequency step in the figures is 34 Hz.

4.2 Effects of spacing

In order to investigate the effects of locations of two PZTs in one Bi-link cell on wave propagation properties of the investigated metamaterial, spacing between two PZTs in one Bi-link cell is considered as a variable *ls* in this section. There are four different sub-methods for the PZT position adjustment as shown in Figure 5. In the reference SSDI Bi-link periodic cell, two identical PZTs are symmetrically bonded on the beam element. The initial value of the variable *ls* is equal to 2*lm* as shown in Figure 1. When two identical PZTs symmetrically approach each other, the spacing *ls* between two PZTs ($0 \leqslant ls \leqslant 2lm$) is reduced from *2lm* to *4lm/3* and then to *2lm/3* as shown in Figure 5(a). Figure 6(a-1) shows the corresponding wave attenuation performance of the investigated metamaterial in the open circuit condition. Figure 6(b-1) shows the corresponding wave attenuation performance of the investigated metamaterial in the SSDI Bi-link condition. In the reference SSDI Bi-link periodic cell, when one PZT moves unilaterally toward the other, the spacing between two PZTs ($0 \leqslant ls \leqslant 2lm$) is reduced from *2lm* to *4lm/3* and then to *2lm/3* as shown in Figure 5(c). Figure 6 (a-2) shows that the corresponding wave attenuation performance of the investigated metamaterial when the Bi-link periodic cell is in the open circuit

condition. Figure 6 (b-2) shows that the corresponding wave attenuation performance of the investigated metamaterial in the SSDI Bi-link condition.

By comparison, it can be seen that the curves in Figure 6 (a) and (b) corresponding to two cases as shown in Figure 5 (a) and (c) change in the same way. The possible reason for this is that the spacing between two piezoelectric patches in each Bi-link periodic cell greatly affects the band gap characteristics of such piezoelectric meta-structure. Changing the spacing between two piezoelectric patches in each Bi-link periodic cell may alter the degree of electromechanical coupling within one Bi-link periodic cell. Whether two identical PZTs symmetrically approaching each other or one PZT moving unilaterally toward the other, the specific positions of two piezoelectric patches in one Bi-link periodic cell does not affect the bandgap locations and amplitudes on the condition that the spacing between two PZTs is constant.

Specifically, in the open circuit condition, the two generated Bragg-type band gaps in the frequency ranges [7.2 kHz, 8.1 kHz]∪[29 kHz, 32 kHz] begin to move towards the low frequency range and their maximum amplitude goes down gradually with the decrease of the spacing between two PZTs. In the SSDI Bi-link condition, the resonant-type band gap performance using the SSDI Bi-link method become obviously better in the frequency range [17 kHz, 30 kHz], but get worse in the other

frequency ranges with the decrease of the spacing between two PZTs. This may denote that the SSDI resonant-type band gap exhibits good coupling effects with the second Bragg-type band gap since the second Bragg-type band gap gradually moves into the lower frequency range [17 kHz, 30 kHz] and the maximum amplitude of second Bragg-type band gap is just slowly reduced with the decrease of the spacing between two PZTs.

When two identical PZTs symmetrically move away from each other in one periodic cell, the spacing *ls* between two PZTs ($2lm \leqslant ls \leqslant 4lm$) is increased from *2lm* to *7lm/3* or *8lm/3* as shown in Figure 5(b). Figure 6 (c-1) shows that the corresponding wave attenuation performance of the investigated meta-structure in the open circuit condition. Figure 6 (d-1) shows that the corresponding wave attenuation performance of the investigated metamaterial in the SSDI-Bi-link condition. In the reference SSDI Bi-link periodic cell, when one PZT moves unilaterally toward the other ($2lm \leqslant ls \leqslant 3lm$), the spacing between two PZTs is reduced from *2lm* to *4lm/3* and then to *2lm/3* as shown in Figure 5(d). Figure 6 (c-2) shows that the corresponding wave attenuation performance of the investigated meta-structure in the open circuit condition. Figure 6 (d-2) shows that the corresponding wave attenuation performance of the investigated metamaterial in the SSDI-Bi-link condition.

By comparison, similar with Figure 6(a) and Figure 6 (b), it can be seen that the curves in Figure 6 (c) and Figure 6 (d) corresponding to two cases as shown in Figure 5(b) and Figure 5(d) change in the same way. The possible reason for this is also similar with the above case when decreasing the spacing between two piezoelectric patches. Specifically, in the open circuit condition, two Bragg-type band gaps move forward to the relative higher frequency range as shown in Figure 6 (c). Therefore, increasing the spacing between two PZTs can move the Bragg-type band gaps towards higher frequency domain. Furthermore, as shown in Figure 6(d), the resonant-type band gap performance using the SSDI Bi-link method become better in the frequency ranges [0 kHz, 7 kHz] and [16.5 kHz, 17.7 kHz], but get worse in the other frequency ranges with the increase of the spacing between two PZTs. It is interesting that the trough in the frequency range [16.5 kHz, 17.7 kHz] for the resonant-type band gap performance using the SSDI Bi-link method becomes a peak with the increase of the spacing between two PZTs. This phenomenon may be explained that there is no coupling effects between the SSDI resonant-type band gap and the Bragg-type band gap in the relatively high frequency range of the investigated frequency domain [0 Hz, 35kHz] since the second Bragg-type band gap moves towards the higher frequency range with the increase of the spacing between two PZTs as shown in Figure 6(c).

Overall, for the effects of PZT spacing adjustment on the open circuit condition, compared with Bragg-type bandgaps of the initial metamaterial including reference Bi-link periodic cells, decreasing the spacing between two piezoelectric patches within every Bi-link periodic cell can move Bragg-type bandgaps towards the lower frequency range and attenuates the maximal attenuation coefficient amplitude of Bragg-type bandgaps, while increasing the PZT spacing can move Bragg-type bandgaps towards the higher frequency range and improves the maximal amplitude of Bragg-type bandgaps.

For the effects of PZT spacing adjustment on the SSDI Bi-link condition, compared with SSDI resonant-type bandgaps of the initial metamaterial including reference Bi-link periodic cells, decreasing the spacing between two PZT patches attenuates the attenuation coefficient amplitude of SSDI resonant-type bandgaps in the low broadband frequency range [0 kHz, 7.2 kHz], and improve the attenuation coefficient amplitude of SSDI resonant-type bandgaps in the high broadband frequency range [16.5 kHz, 29 kHz]. While increasing the spacing between two PZT patches is the opposite of decreasing it in the low broadband frequency range [0 kHz, 7.2 kHz] and the high broadband frequency range [16.5 kHz, 29 kHz]. In addition, wave attenuation performance in the intermediate frequency band [7.2 kHz, 16.5 kHz] is weakened no matter the PZT spacing is decreased or increased.

It can also be considered that the change of the spacing between two PZTs induces one kind of an aperiodicity in each Bi-link periodic cell of the global structure. Such aperiodicity by affecting the Bragg-type band gap characteristics helps to selectively increase or decrease the effectiveness of the SSDI Bi-link band gap [50].

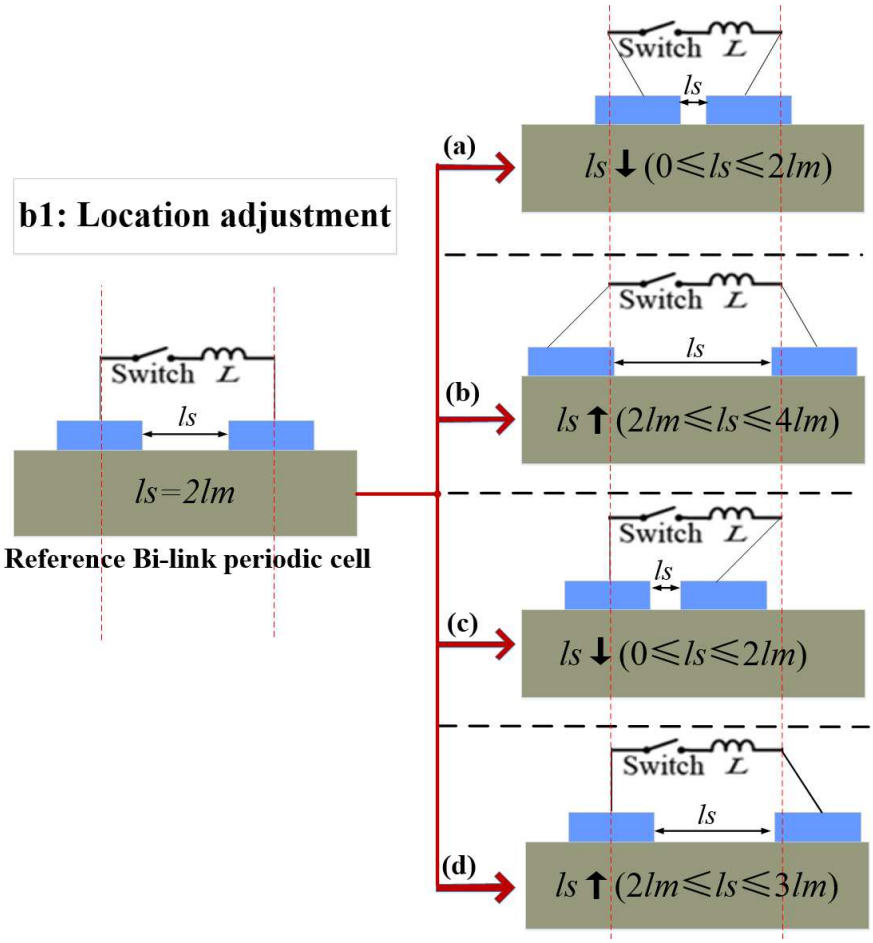

Figure 5 (a) Two identical PZTs symmetrically approach each other; (b) two identical PZTs symmetrically move away from each other; (c) one PZT moves unilaterally toward the other one; (d) one PZT moves unilaterally away from the other one.

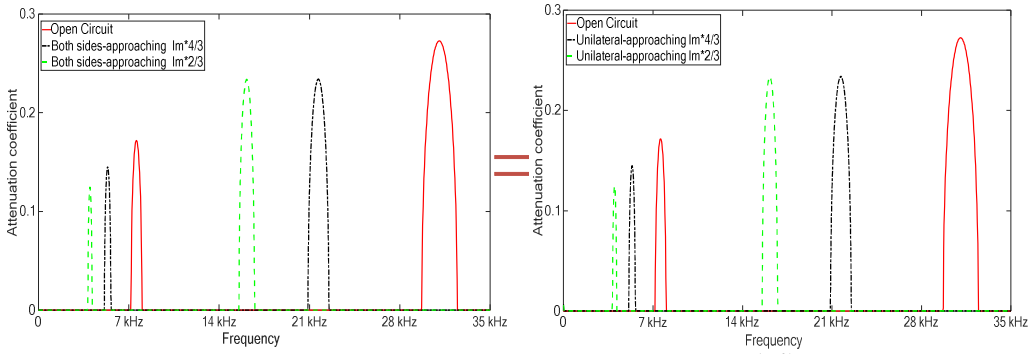

(a-1) **(a-2)**

(a)

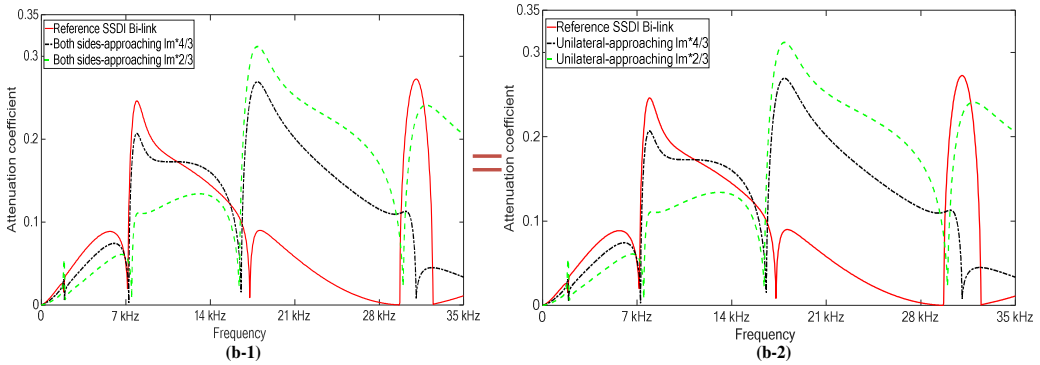

(b-1) **(b-2)**

(b)

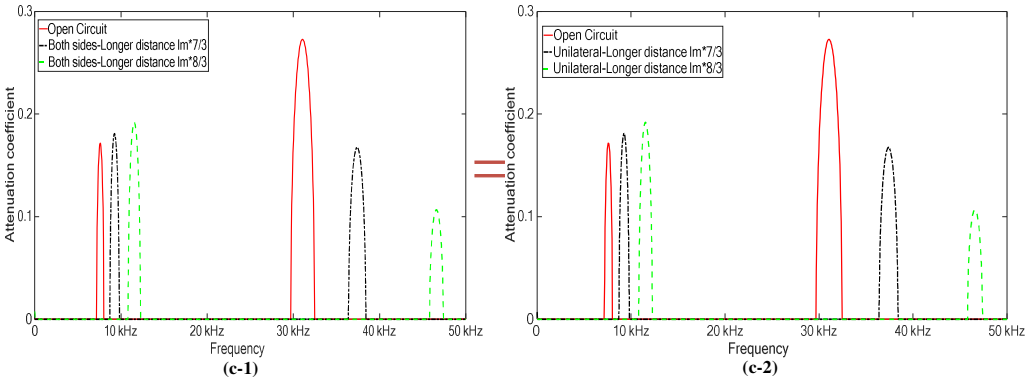

(c-1) **(c-2)**

(c)

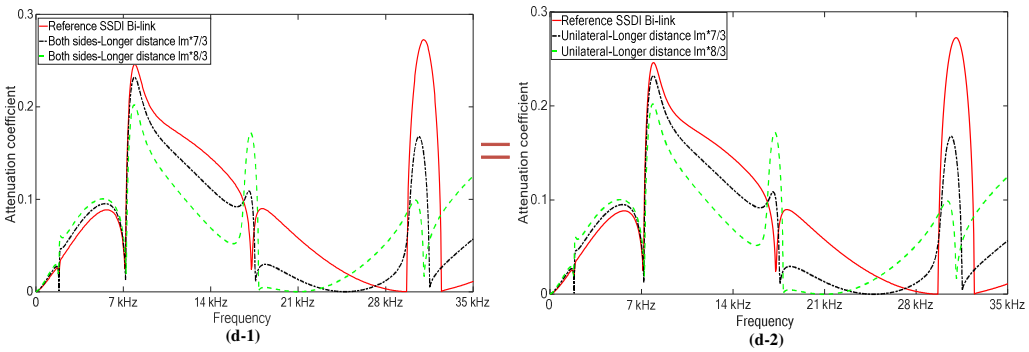

(d)

Figure 6 (a) Wave attenuation performance of the investigated metamaterial in the open circuit condition in the both-sides-approaching methods and the unilateral-approaching methods; (b) wave attenuation performance of the investigated metamaterial in the open circuit condition in the both-sides-moving away methods and the unilateral-moving away methods; (c) wave attenuation performance of the investigated metamaterial in the both-sides-approaching methods and the unilateral-approaching methods; (d) wave attenuation performance of the investigated metamaterial in the both-sides-moving away methods and the unilateral-moving away methods. The frequency step in the figures is 34 Hz.

4.3 Effects of the PZT lengths

The length of two PZTs in one Bi-link cell is considered as a variable l_{p1} or l_{p2} in this section. There are five sub-methods for investigating the effects of the PZT length change as shown in Figure 7. In the reference SSDI Bi-link periodic cell, the PZTs have the same length l_p:

$$l_{p1} = l_{p2} = l_p \tag{29}$$

The PZT length increase/decrease denotes that the increase/decrease of the involved active electromechanical materials and the stiffness of the structure. The effects of the PZT length increase/decrease on wave attenuation performance of the investigated metamaterial are shown in Figure 8. For the open circuit condition, as shown in Figure 8 (a), two generated Bragg-type band gaps begin to move towards the higher frequency band with the increase of the length of one PZT ($l_{p1}=l_p$; $l_p \leqslant l_{p2}<3lm+l_p$) corresponding to Figure 7(a). A small band gap appears between two original Bragg-type band gaps. In such case, the maximum amplitude of first Bragg-type band gap becomes larger, while that of second Bragg-type band gap is gradually reduced. With the decrease of the length of one PZT ($l_{p1}=l_p$; $0 \leqslant l_{p2}<l_p$) corresponding to Figure 7(b), two generated Bragg-type band gaps begin to move towards the lower frequency range as shown in Figure 8 (c). In addition, there is a small new Bragg-type band gap generated around 15 kHz. For the SSDI Bi-link

method, the increase of the length of one PZT can enhance the overall wave attenuation performance of the investigated meta-structure in the frequency range [0 Hz, 30 kHz] as shown in Figure 8(b), while such performance can be weakened by the decrease of the PZT length in the same frequency range [0 Hz, 30 kHz] as shown in Figure 8(d).

The possible reason for such phenomenon is that increasing the length of one PZT can not only enhance the first Bragg-type band gap in the frequency range [0 Hz, 30 kHz], but also enhance the coupling effects between the SSDI resonant-type band gap and the Bragg-type band gap. While the second Bragg-type band gap moves towards the higher frequency range which is out of the investigated frequency domain [0 Hz, 35 kHz] with the increase of one PZT length, and thus there is no band gap coupling effects within the frequency range [30 kHz, 35 kHz]. Therefore, wave attenuation performance of the metamaterial in the SSDI Bi-link condition are weakened in the frequency range [30 kHz, 35 kHz] with the increase of one PZT length. In addition, decreasing the length of one PZT length denotes the reduction of the stiffness of the structure and piezoelectric material, which leads that the electromechanical coupling between the PZTs and the substructure is weakened. And thus, wave attenuation performance of the structure in the SSDI Bi-link condition is reduced with the decrease of the length of one PZT.

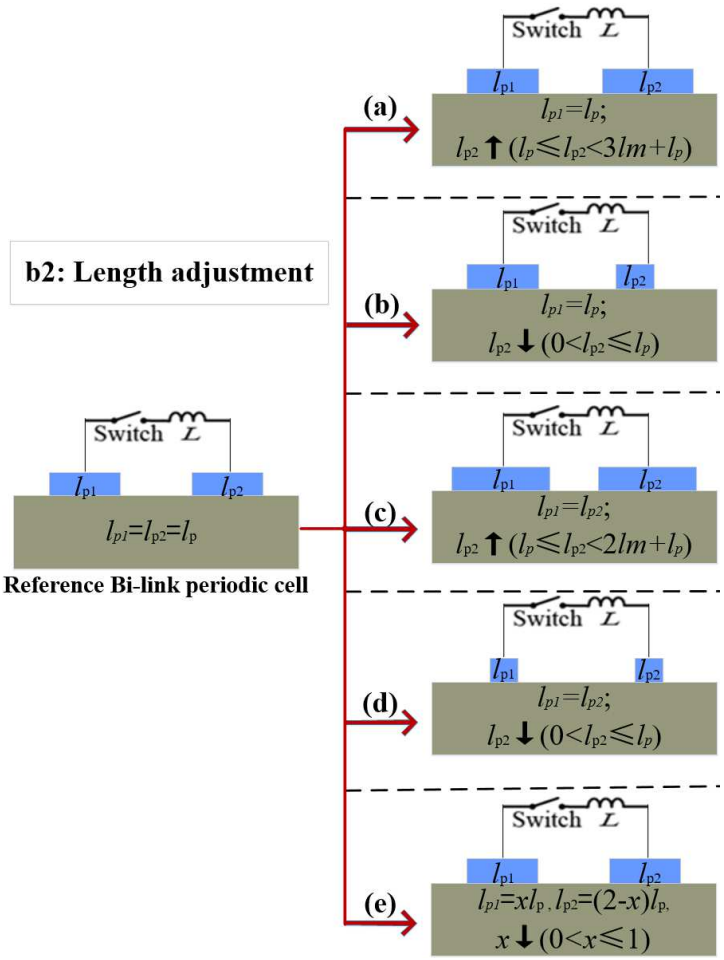

Figure 7 (a) Increasing the length of one of two PZTs (l_{p1}=l_p; l_p≤ l_{p2}<3lm+l_p); (b) decreasing the length of one of two PZTs (l_{p1}=l_p; 0≤ l_{p2}<l_p); (c) increasing the length of two PZTs which have the same length (l_{p1}=l_{p2}; l_p≤l_{p2}<2lm+l_p); (d) decreasing the length of two PZTs which have the same length (l_{p1}=l_{p2}; 0<l_{p2}≤l_p) ; (e) On the condition that the sum of the length of two PZTs are equal to 2l_p, decreasing one PZT length and increasing the other one PZT length (l_{p1}=xl_p; l_{p2}=(2-x)l_p; 0<x≤1).

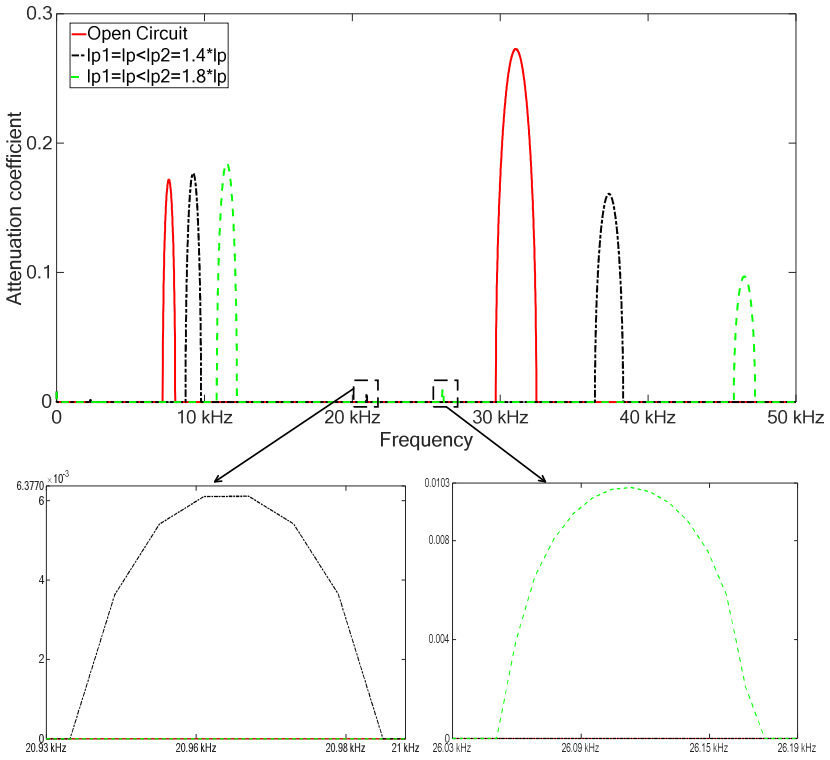
Open Circuit
lp1=lp<lp2=1.4*lp
lp1=lp<lp2=1.8*lp
Attenuation coefficient
Frequency
0
10 kHz
20 kHz
30 kHz
40 kHz
50 kHz
0.3
0.2
0.1
6.3770 ×10^-3
20.93 kHz
20.96 kHz
20.98 kHz
21 kHz
0.0103
0.008
0.004
26.03 kHz
26.09 kHz
26.15 kHz
26.19 kHz

(a)

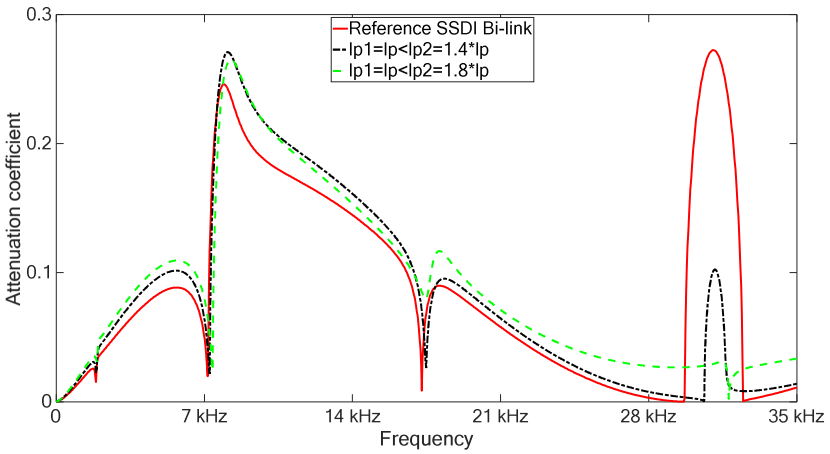
Reference SSDI Bi-link
lp1=lp<lp2=1.4*lp
lp1=lp<lp2=1.8*lp
Attenuation coefficient
Frequency
0
7 kHz
14 kHz
21 kHz
28 kHz
35 kHz
0.3
0.2
0.1

(b)

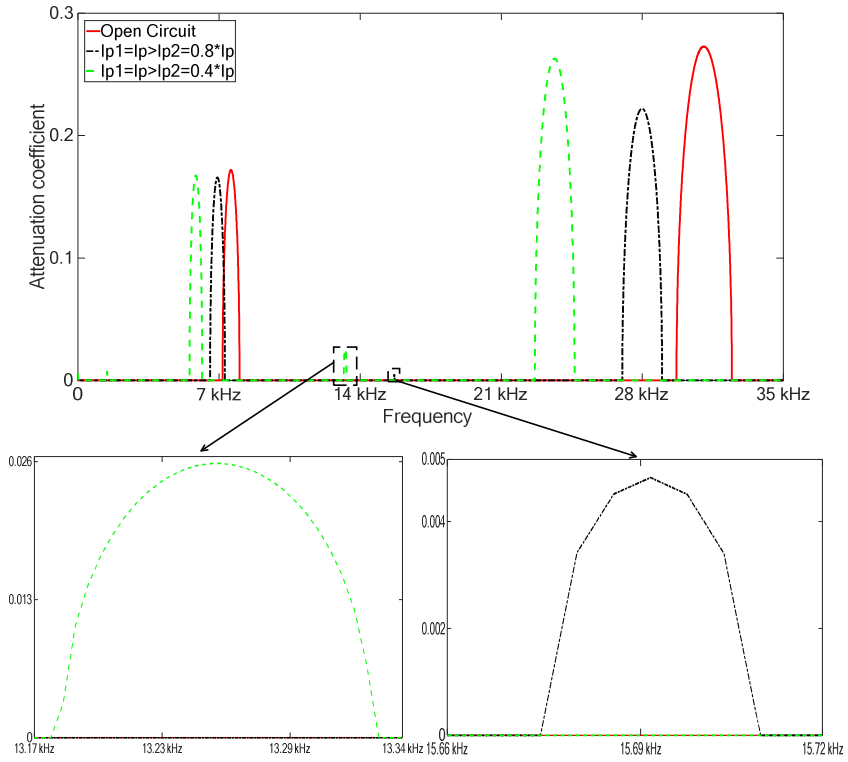

(c)

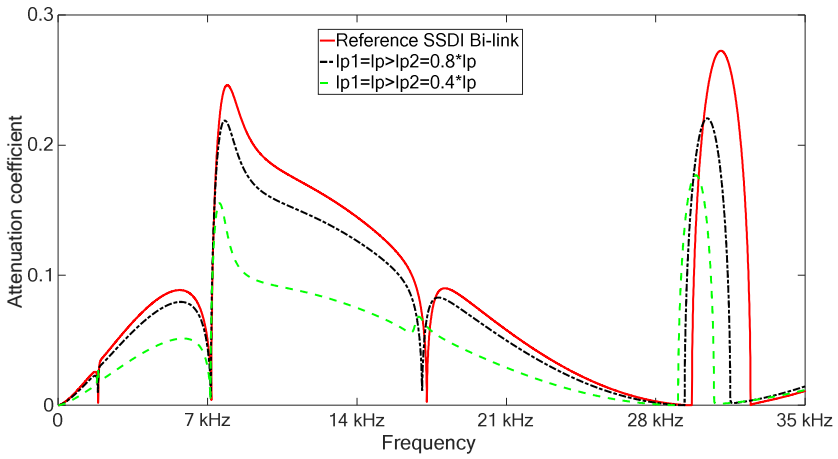

(d)

Figure 8 (a) Wave attenuation performance of the investigated metamaterial in the open circuit condition with the increase of the length of one PZT corresponding to the sub-method as shown in Figure 7(a); (b) wave attenuation performance of the investigated metamaterial with the

increase of the length of one PZT corresponding to the sub-method as shown in Figure 7(a); (c) wave attenuation performance of the investigated metamaterial in the open circuit condition with the decrease of the length of one PZT corresponding to the sub-method as shown in Figure 7(b); (d) wave attenuation performance of the investigated metamaterial with the decrease of the length of one PZT corresponding to the sub-method as shown in Figure 7(b). The frequency step in the figures is 34 Hz, while the frequency step in the zoom areas of the figures is 4.2 Hz.

Increasing the lengths of both PZTs ($l_{p1}=l_{p2}$; $l_p \leqslant l_{p2}<2lm+l_p$) corresponding to Figure 7(c) yields a shift of the two generated Bragg-type band gaps towards the higher frequency range (Figure 9 (a)), while their decrease ($l_{p1}=l_{p2}$; $0<l_{p2}\leqslant l_p$) corresponding to Figure 7(d) moves these band gaps towards the lower frequency range (Figure 9 (c)). Compared with the cases of increasing/decreasing the length of two PZTs, the cases of increasing/decreasing one PZT length can more greatly change the positions of the Bragg-type band gaps as shown in Figure 8(a) and (c). For the SSDI Bi-link method, the wave attenuation performance of the investigated metamaterial in the frequency range [0 Hz, 7 kHz] can be enhanced by increasing these lengths as shown in Figure 9 (b). However, the increase of the lengths of two identical PZTs does not yield

an improvement of wave attenuation performance of the investigated metamaterial in the whole frequency range. The wave attenuation performance when the lengths of two identical PZTs are equal to $1.4l_p$ is better than that when the lengths of two identical PZTs are equal to $1.8l_p$ in the frequency range [7 kHz, 30 kHz] as shown in Figure 9 (b). In addition, Figure 9 (d) shows that wave attenuation performance of the investigated metamaterial is weakened by the decrease of the lengths of two identical PZTs in the frequency range [0 Hz, 30 kHz]. These trade-offs may be explained by the existence of an optimal length that maximizes the structural electromechanical coupling coefficient of the cell.

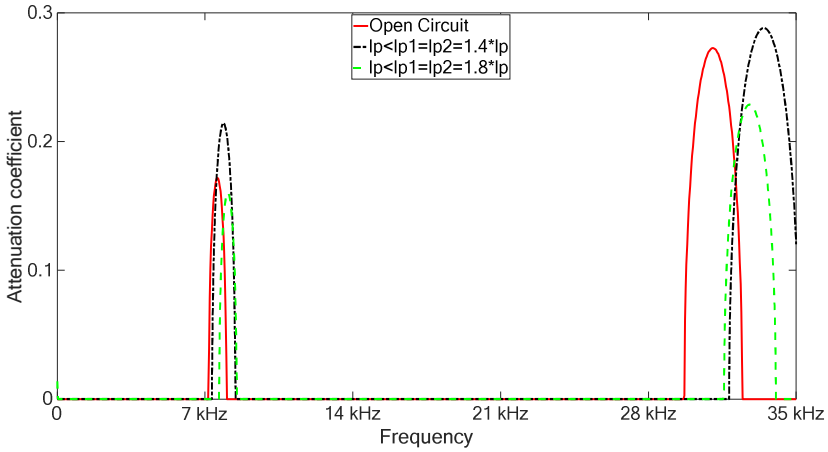

(a)

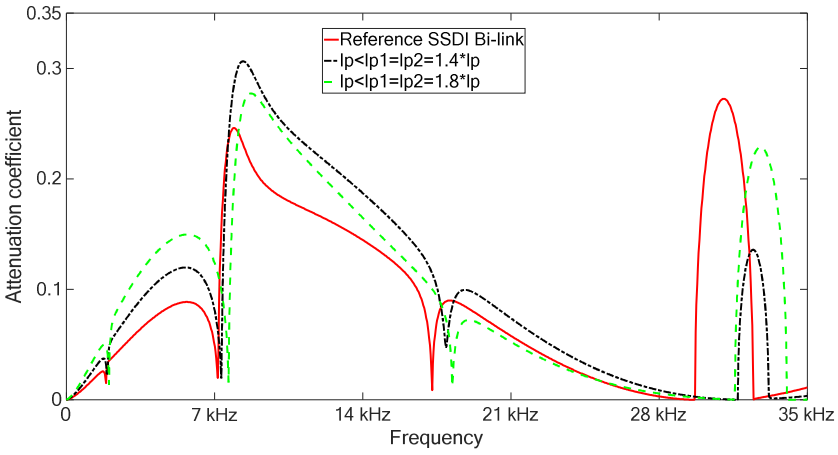
Reference SSDI Bi-link
lp<lp1=lp2=1.4*lp
lp<lp1=lp2=1.8*lp
Attenuation coefficient
Frequency
0
0.1
0.2
0.3
0.35
0
7 kHz
14 kHz
21 kHz
28 kHz
35 kHz

(b)

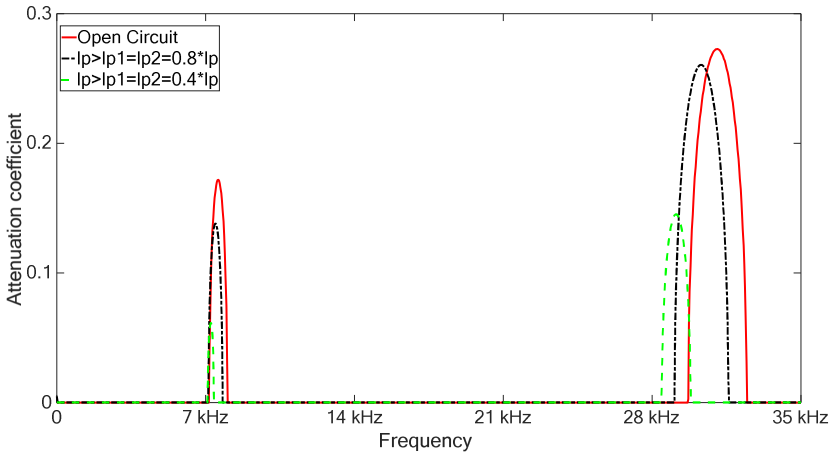
Open Circuit
lp>lp1=lp2=0.8*lp
lp>lp1=lp2=0.4*lp
Attenuation coefficient
Frequency
0
0.1
0.2
0.3
0
7 kHz
14 kHz
21 kHz
28 kHz
35 kHz

(c)

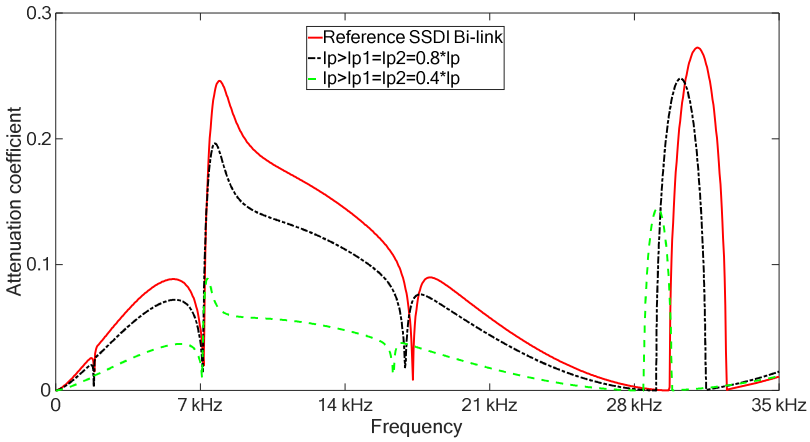
Reference SSDI Bi-link
lp>lp1=lp2=0.8*lp
lp>lp1=lp2=0.4*lp
Attenuation coefficient
Frequency
0
0.1
0.2
0.3
0
7 kHz
14 kHz
21 kHz
28 kHz
35 kHz

(d)

Figure 9 (a) Wave attenuation performance of the investigated metamaterial in the open circuit condition with the increase of both PZT lengths corresponding to the sub-method as shown in Figure 7(c); (b) wave attenuation performance of the investigated metamaterial with the increase of both PZT lengths corresponding to the sub-method as shown in Figure 7(c); (c) wave attenuation performance of the investigated metamaterial in the open circuit condition with the decrease of both PZT lengths corresponding to the sub-method as shown in Figure 7(c); (d) wave attenuation performance of the investigated metamaterial with the decrease of both PZT lengths corresponding to the sub-method as shown in Figure 7(c). The frequency step in the figures is 34 Hz.

When the length of one PZT decreases smaller than l_p and the length of the other one PZT in one periodic cell increases larger than l_p on the condition that the sum of the lengths of two PZTs is equal to $2l_p$ as shown in Figure 7(e), wave attenuation performance of the investigated metamaterial in the open circuit and SSDI Bi-link conditions is obtained as shown in Figure 10. With the length decrease of the PZT1 and the length decrease of the PZT2, the electromechanical coupling between the PZT1 and the beam substructure is attenuated and that between the PZT2 and the beam substructure is enhanced compared to the investigated metamaterial in the reference case. Specifically, the maximum amplitudes

of two generated Bragg-type band gaps are reduced, and the locations of two Bragg-type band gaps move towards the higher frequency band in the open circuit condition as shown in Figure 10(a). In the SSDI Bi-link condition as shown in Figure 10(b), wave attenuation performance in the global frequency domain except the frequency range [1.8 kHz, 2 kHz] is gradually reduced with the length decrease of the PZT1 and the length decrease of the PZT2. The trough gradually changes to a peak in the frequency range [1.8 kHz, 2 kHz]. Therefore, such sub-method for the SSDI Bi-link method cannot help to improve wave attenuation performance of the structure in the investigated frequency domain. The possible reason for this is that the band gap hybridization effects are greatly weakened in the investigated frequency domain due to the reduction of the Bragg-type band gaps and the locations of Bragg-type band gaps shifting to the higher frequency range.

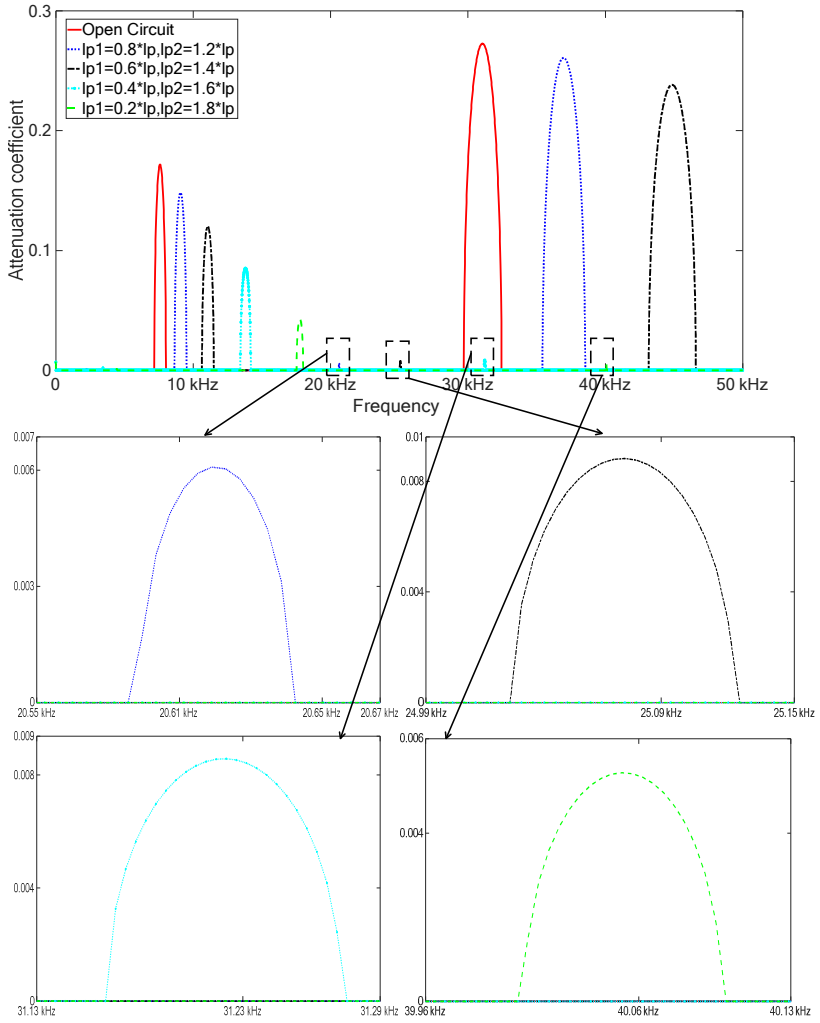
Open Circuit
lp1=0.8*lp,lp2=1.2*lp
lp1=0.6*lp,lp2=1.4*lp
lp1=0.4*lp,lp2=1.6*lp
lp1=0.2*lp,lp2=1.8*lp
Attenuation coefficient
Frequency
0
10 kHz
20 kHz
30 kHz
40 kHz
50 kHz
20.55 kHz
20.61 kHz
20.65 kHz
20.67 kHz
24.99 kHz
25.09 kHz
25.15 kHz
31.13 kHz
31.23 kHz
31.29 kHz
39.96 kHz
40.06 kHz
40.13 kHz

(a)

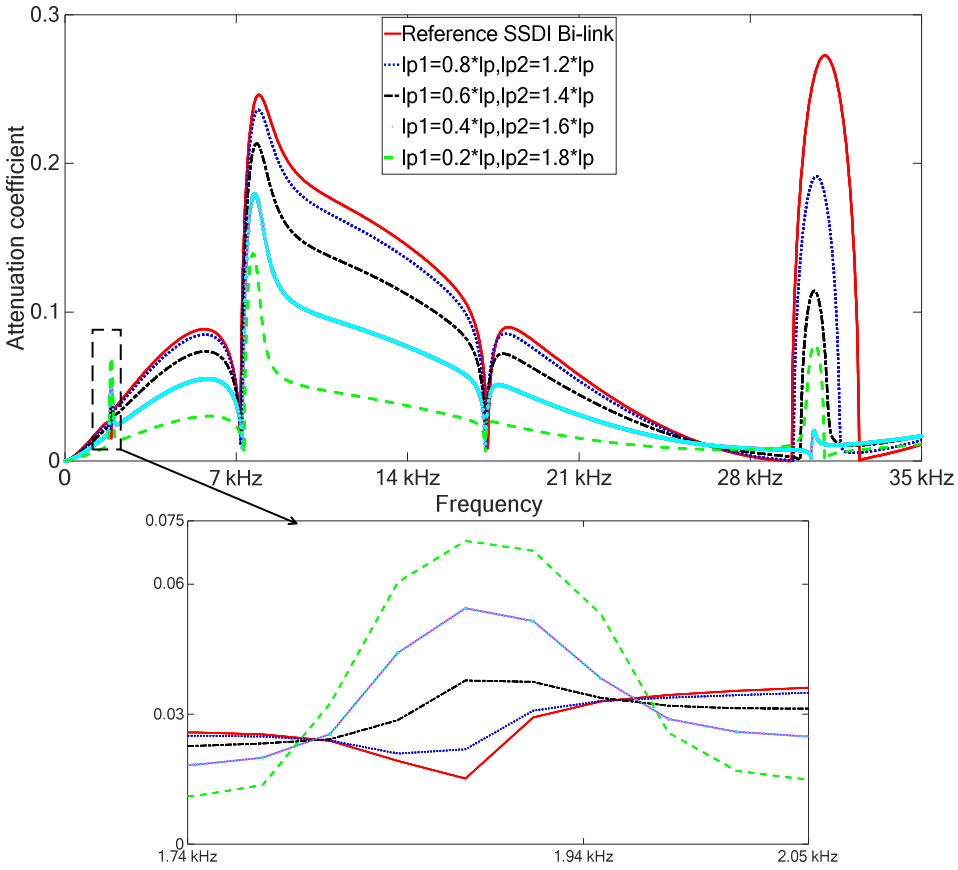

(b)

Figure 10 (a) Wave attenuation performance of the investigated metamaterial in the open circuit condition with the increase of one PZT length and the decrease of the other one PZT length corresponding to Figure 7(e): x=0.8,0.6,0.4,0.2; (b) wave attenuation performance of the investigated metamaterial with the increase of one PZT length and the decrease of the other one PZT length corresponding to Figure 7(e): x=0.8,0.6,0.4,0.2. The frequency step in the figures is 34 Hz, while the frequency step in the zoom areas of the figures is 4.2 Hz.

4.4 Effects of the PZT thicknesses

In order to investigate the effects of the thicknesses of two PZTs in one Bi-link cell on wave propagation properties of the investigated meta-structure, the thickness of two PZTs in one Bi-link cell is considered as a variable t_{p1} or t_{p2} in this section. There are five sub-methods for investigating the effects of the PZT thickness change as shown in Figure 11. In the reference Bi-link periodic cell, two identical PZTs have the same thickness t_p:

$$t_{p1} = t_{p2} = t_p \tag{30}$$

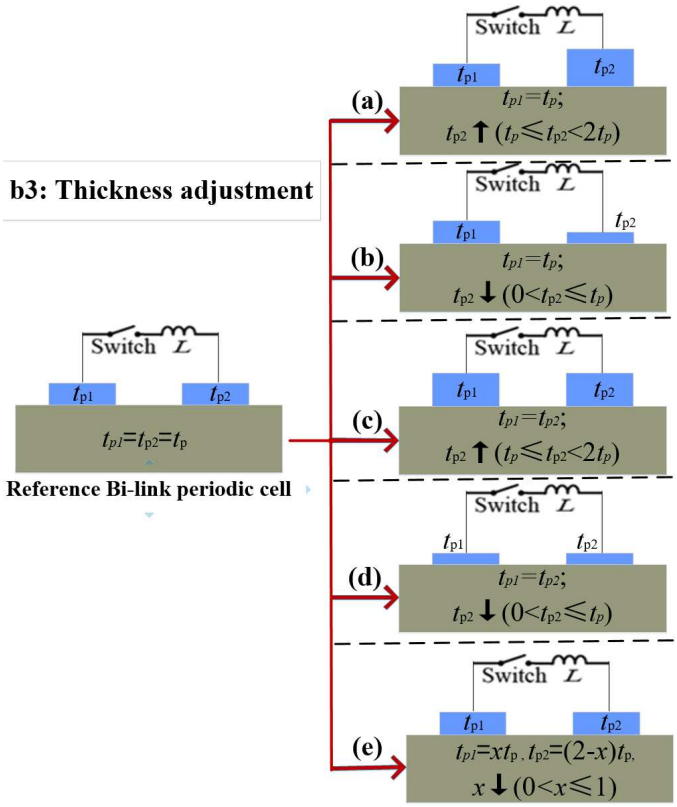

Figure 11 (a) Increasing the thickness of one of two PZTs in one Bi-link periodic cell ($t_{p1}=t_p$; $t_p \leq t_{p2} < 2t_p$); (b) decreasing the thickness of one of

two PZTs in one Bi-link periodic cell ($t_{p1}=t_p$; $0<t_{p2}\leq t_p$); (c) increasing the thickness of both PZTs which have the same thickness ($t_{p1}=t_{p2}$; $t_p\leq t_{p2}<2t_p$); (d) decreasing the thickness of both PZTs which have the same thickness($t_{p1}=t_{p2}$; $0<t_{p2}\leq t_p$); (e) On the condition that the sum of the thickness of two PZTs are equal to $2t_p$, decreasing the thickness of one PZT and increasing the thickness of the other one PZT ($t_{p1}=xt_p$; $t_{p2}=(2-x)t_p$; $0<x\leq 1$).

Increasing or decreasing the PZT thickness in one periodic cell denotes that more or less piezoelectric materials are introduced in one periodic cell, which greatly affects the electromechanical coupling coefficient of the structure (and not necessarily increasing it). Due to the change of PZT thickness, the neutral axis position and the local strain/stress of one periodic cell will be altered. When the thickness of one of two PZTs is larger/smaller than t_p as shown in Figure 11(a) and (b), the effects of the PZT thickness increase/decrease are shown in Figure 12. In open circuit condition, the first Bragg-type band gap [7.2 kHz, 8.1 kHz] is enhanced by increasing the PZT thickness, and the second Bragg-type band gap [29 kHz, 32 kHz] is weakened due to the increase of the thickness as shown in Figure 12 (a). In addition, two additional small Bragg-type band gaps are generated around 1.8 kHz and 17 kHz. Such trade-off performance may be explained by the existence of an optimal PZT thickness that

maximizes the structural electromechanical coupling coefficient of the periodic cell. With the decrease of the thickness of one PZT, the two original Bragg-type band gaps are weakened and a new small Bragg-type band gap is generated around 17 kHz as shown in Figure 12(c). For the investigated SSDI Bi-link method, the wave attenuation performance of the investigated metamaterial improves in the whole investigated frequency range as the one PZT thickness increases as shown in Figure 12 (b), while they are reduced by the decrease of the thickness (Figure 12 (d)).

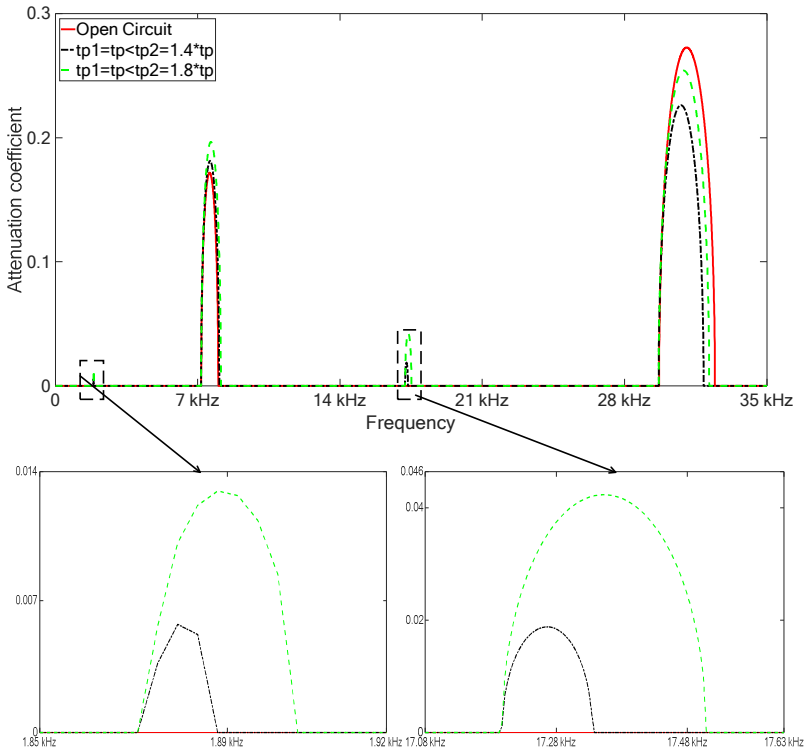

(a)

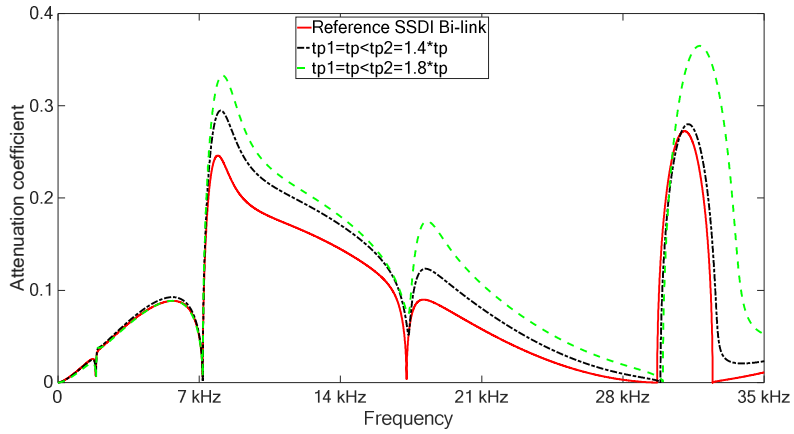
Reference SSDI Bi-link
tp1=tp<tp2=1.4*tp
tp1=tp<tp2=1.8*tp
Attenuation coefficient
0.4
0.3
0.2
0.1
0
0
7 kHz
14 kHz
21 kHz
28 kHz
35 kHz
Frequency

(b)

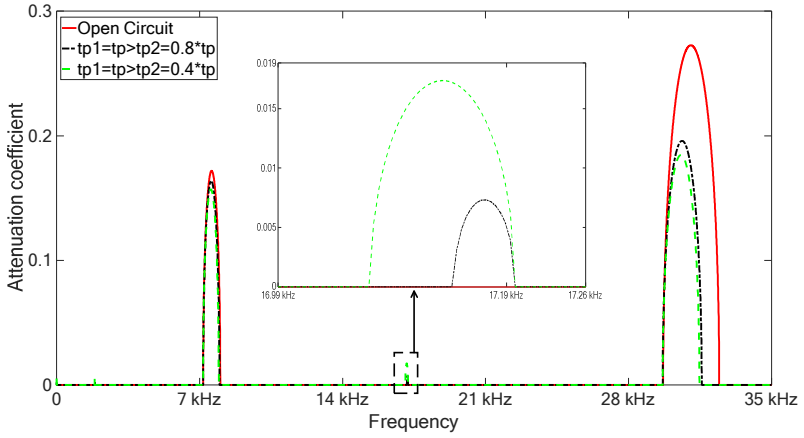
Open Circuit
tp1=tp>tp2=0.8*tp
tp1=tp>tp2=0.4*tp
0.019
0.015
0.01
0.005
0
16.99 kHz
17.19 kHz
17.26 kHz
Attenuation coefficient
0.3
0.2
0.1
0
0
7 kHz
14 kHz
21 kHz
28 kHz
35 kHz
Frequency

(c)

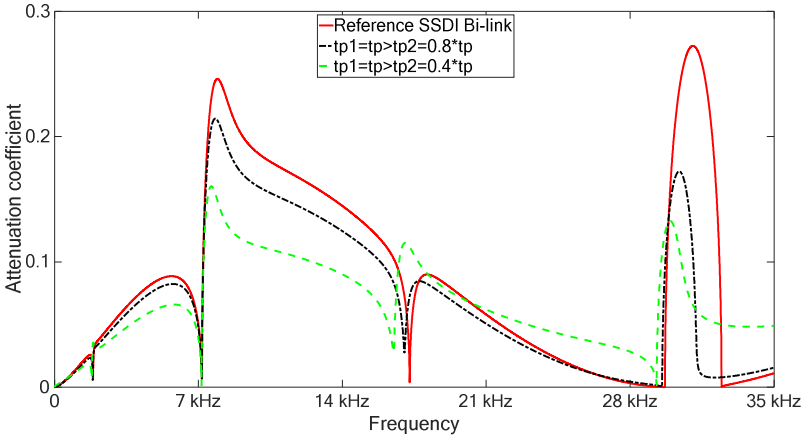
Reference SSDI Bi-link
tp1=tp>tp2=0.8*tp
tp1=tp>tp2=0.4*tp
Attenuation coefficient
0.3
0.2
0.1
0
0
7 kHz
14 kHz
21 kHz
28 kHz
35 kHz
Frequency

(d)

Figure 12 (a) Wave attenuation performance of the investigated metamaterial in the open circuit condition with the increase of one PZT thickness; (b) wave attenuation performance of the investigated metamaterial with the increase of one PZT thickness; (c) wave attenuation performance of the investigated metamaterial in the open circuit condition with the decrease of one PZT thickness; (d) wave attenuation performance of the investigated metamaterial with the decrease of one PZT thickness. The frequency step in the figures is 34 Hz, while the frequency step in the zoom areas of the figures is 4.2 Hz.

When both thicknesses are changed (Figure 11(c) and (d)), the effects of their increase/decrease are shown in Figure 13. In the open circuit condition, the two original Bragg-type band gaps [7.2 kHz, 8.1 kHz] ∪ [29 kHz, 32 kHz] are enlarged by increasing the thicknesses (Figure 13 (a)), while Figure 13 (c) shows that the thicknesses decrease reduces the two original Bragg-type band gaps. For the SSDI Bi-link method, Figure 13 (b) shows that increasing the thickness both of two PZTs is beneficial for improving wave attenuation performance in the whole investigated frequency range, while Figure 13 (d) shows that decreasing the thickness has negative effects on these performance.

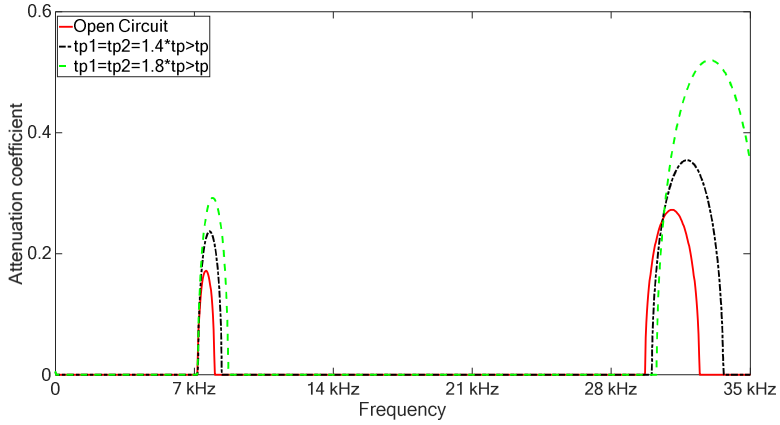
Open Circuit
tp1=tp2=1.4*tp>tp
tp1=tp2=1.8*tp>tp
Attenuation coefficient
0.6
0.4
0.2
0
0
7 kHz
14 kHz
21 kHz
28 kHz
35 kHz
Frequency

(a)

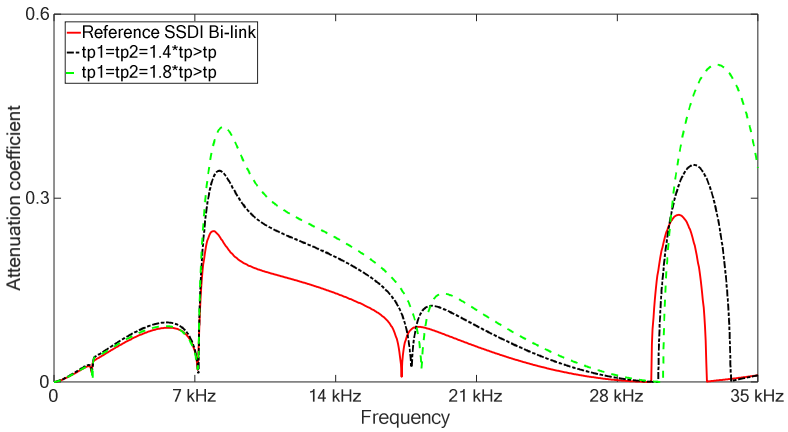
Reference SSDI Bi-link
tp1=tp2=1.4*tp>tp
tp1=tp2=1.8*tp>tp
Attenuation coefficient
0.6
0.3
0
0
7 kHz
14 kHz
21 kHz
28 kHz
35 kHz
Frequency

(b)

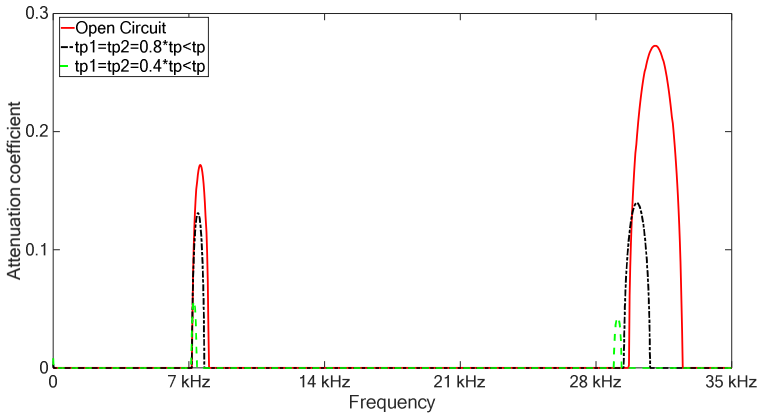
Open Circuit
tp1=tp2=0.8*tp<tp
tp1=tp2=0.4*tp<tp
Attenuation coefficient
0.3
0.2
0.1
0
0
7 kHz
14 kHz
21 kHz
28 kHz
35 kHz
Frequency

(c)

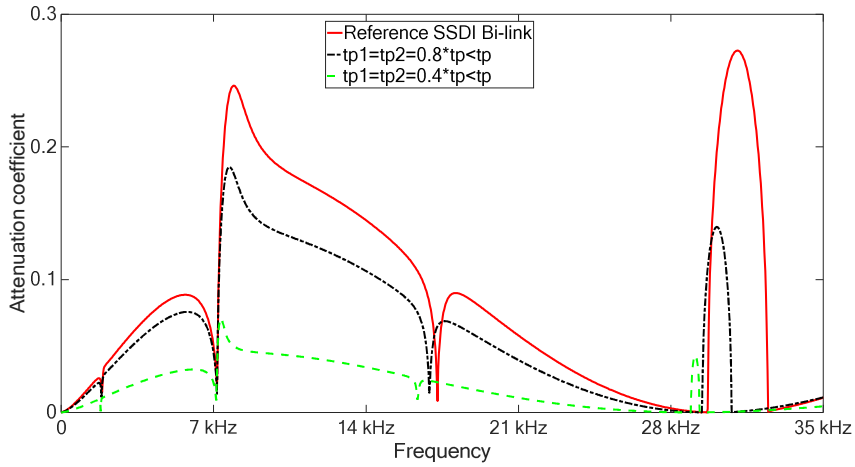

(d)

Figure 13 (a) Wave attenuation performance of the investigated metamaterial in open circuit condition with the increase of both PZT thicknesses; (b) wave attenuation performance of the investigated metamaterial with the increase of both PZT thicknesses; (c) wave attenuation performance of the investigated metamaterial in open circuit condition with the decrease of both PZT thicknesses; (d) wave attenuation performance of the investigated metamaterial with the decrease of both PZT thicknesses. The frequency step in the figures is 34 Hz.

When the thickness of one PZT decreases smaller than t_p and the thickness of the other one PZT in one periodic cell increases larger than t_p on the condition that the sum of the thicknesses of two PZTs is equal to $2t_p$ as shown in Figure 11(e)，wave attenuation performance of the investigated metamaterial under different electrical boundary conditions is shown in Figure 14. In the open circuit condition as shown in Figure

14(a), the maximal attenuation coefficients of two original Bragg-type band gaps are gradually reduced with the thickness decrease of the PZT1 and the thickness increase of the PZT2 in one periodic cell. The higher edge of the first original Bragg-type band gap [7.2 kHz, 8.1 kHz] is reduced from 8.1 kHz to 7.6 kHz. The location of the second original Bragg-type band gap [29 kHz, 32 kHz] globally moves to the left. Additional Bragg-type band gaps are generated in the frequency ranges [1.75 kHz, 1.95 kHz]∪[16.1 kHz, 17.1 kHz] ∪[45 kHz, 50 kHz]. With the thickness decrease of the PZT1 and the thickness increase of the PZT2 in one periodic cell, these new Bragg-type band gaps are greatly enhanced.

For the SSDI Bi-link case as shown in Figure 14(b), wave attenuation performance of the investigated metamaterial are gradually reduced in the frequency ranges [0 kHz, 1.8 kHz]∪[2.0 kHz, 16.5 kHz]. While in the frequency domains [1.8 kHz, 2.0 kHz] ∪[16.5 kHz, 29 kHz]∪[32 kHz, 35 kHz], wave attenuation performance of the investigated metamaterial are gradually enhanced with the thickness decrease of the PZT1 and the thickness increase of the PZT2 in one periodic cell. The possible reason for this is that there exists good band gap hybridization coupling effects between the SSDI resonant-type band gap and two new Bragg-type band gaps in the frequency domains [1.75 kHz, 1.95 kHz]∪[16.1 kHz, 17.1 kHz].

In addition, different from the above frequency ranges, wave attenuation performance of the investigated metamaterial in the second original Bragg-type band gap [29 kHz, 32 kHz] is weakened before it is enhanced. The possible reason for this is that the second Bragg-type band gap is weakened using this sub-method, and the band gap hybridization coupling effects between the SSDI resonant band gap and the second original Bragg-type band gap are attenuated. However, with the decrease of one PZT thickness and the increase of the other one PZT thickness, the third new generated Bragg-type band gap in the frequency domain [45 kHz, 50 kHz] gradually shifts to the left and approaches to the second original Bragg-type band gap as shown in Figure 14(a). The band gap coupling effects between the SSDI resonant-type band gap and the third new generated Bragg-type band gap become enhanced, which improves the wave attenuation performance in the second original Bragg-type band gap.

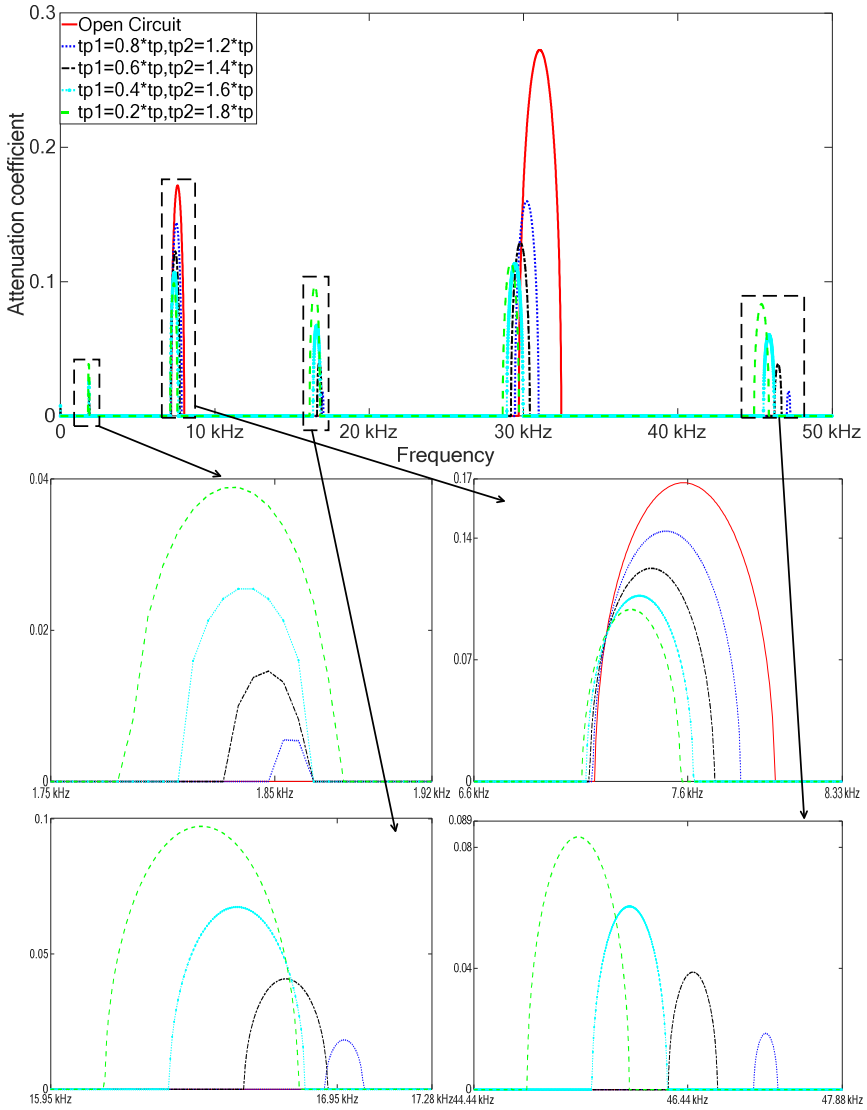
Open Circuit
tp1=0.8*tp,tp2=1.2*tp
tp1=0.6*tp,tp2=1.4*tp
tp1=0.4*tp,tp2=1.6*tp
tp1=0.2*tp,tp2=1.8*tp
Attenuation coefficient
Frequency
0
10 kHz
20 kHz
30 kHz
40 kHz
50 kHz
1.75 kHz
1.85 kHz
1.92 kHz
6.6 kHz
7.6 kHz
8.33 kHz
15.95 kHz
16.95 kHz
17.28 kHz
44.44 kHz
46.44 kHz
47.88 kHz

(a)

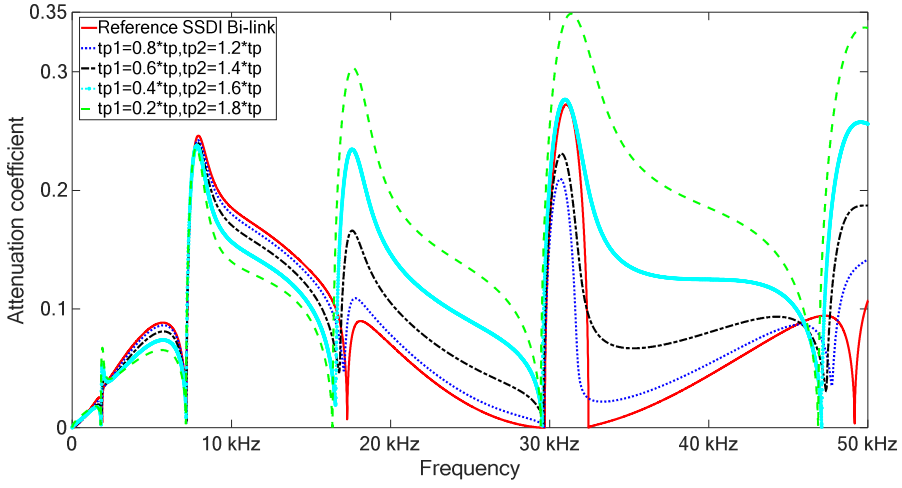
Reference SSDI Bi-link
tp1=0.8*tp,tp2=1.2*tp
tp1=0.6*tp,tp2=1.4*tp
tp1=0.4*tp,tp2=1.6*tp
tp1=0.2*tp,tp2=1.8*tp
Attenuation coefficient
Frequency
0
10 kHz
20 kHz
30 kHz
40 kHz
50 kHz

(b)

Figure 14(a) Wave attenuation performance of the investigated metamaterial in the open circuit condition with the increase of one PZT thickness and the decrease of the other one PZT thickness corresponding to Figure 11(e): x=0.8,0.6,0.4,0.2; (b) wave attenuation performance of the investigated metamaterial with the increase of one PZT thickness and the decrease of the other one PZT thickness corresponding to Figure 11(e): x=0.8,0.6,0.4,0.2. The frequency step in the figures is 34 Hz, while the frequency step in the zoom areas of the figures is 4.2 Hz.

4.5 The effects of the charge coefficient of PZT

In order to investigate the effects of the charge coefficient of two PZTs in one Bi-link cell on wave propagation properties of the investigated metamaterial, the charge coefficient d_{31} of the two PZTs in one Bi-link cell is considered as a variable in this section. There are four sub-methods for investigating the effects of the charge coefficient of PZT as shown in Figure 15. In the reference Bi-link periodic cell, two identical PZTs have the same charge coefficient:

$$d_{31}^{p1} = d_{31}^{p2} = d_{31} \tag{31}$$

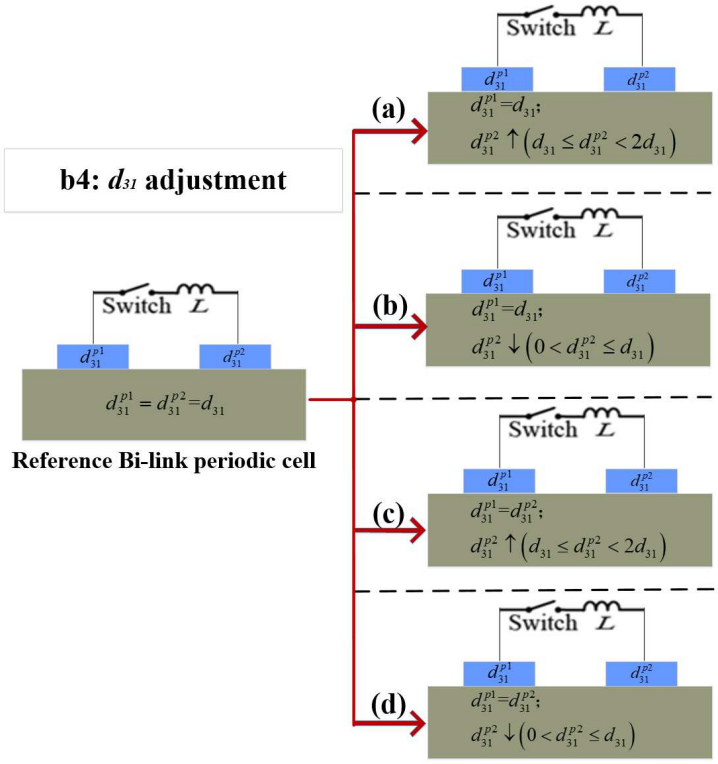

Figure 15 (a) Increasing the charge coefficient of one PZT; (b) decreasing the charge coefficient of one PZT; (c) increasing the charge coefficient of two PZTs which have the same charge coefficient; (d) decreasing the charge coefficient of two PZTs which have the same charge coefficient.

Overall, as shown in Figure 16(a), two original Bragg-type band gaps are enhanced by increasing the charge coefficient of one PZT in open circuit condition. In addition, two new small Bragg-type band gaps are generated around 1.9 kHz and 17 kHz with the increase of the charge coefficient of one PZT. However, there is a special case that the wave attenuation performance of the second original Bragg-type band gap [29 kHz, 32 kHz] is reduced when the charge coefficient of one PZT is equal to $1.3d_{31}$. The

possible reason for this is that the aperiodicity or the defect induced by the increase of the charge coefficient of one PZT is only beneficial to the first Bragg-type band gap enhancement. But it has an offsetting effect on the second Bragg-type band gap. Therefore, electromechanical coupling performance of the investigated structure is generally improved with the increase of the charge coefficient d_{31} of the PZT, but when the increase of the charge coefficient d_{31} of the PZT is relatively small, such increase may not enhance all the Bragg-type band gaps. For the SSDI Bi-link method, as shown in Figure 16(b), increasing the charge coefficient of one PZT can also improve global wave attenuation performance of the investigated structure. Herein, it should be noted that the charge coefficient of the PZT is limited by development of piezoelectric material technology, which cannot be infinitely improved. Accordingly, the effects of the charge coefficient of the PZT on wave attenuation performance are also limited. While Figure 16 (c) and (d) shows that the decrease of the charge coefficient of one PZT attenuates the two original Bragg-type band gaps in open circuit condition, and also reduces the performance in the most of investigated frequency ranges.

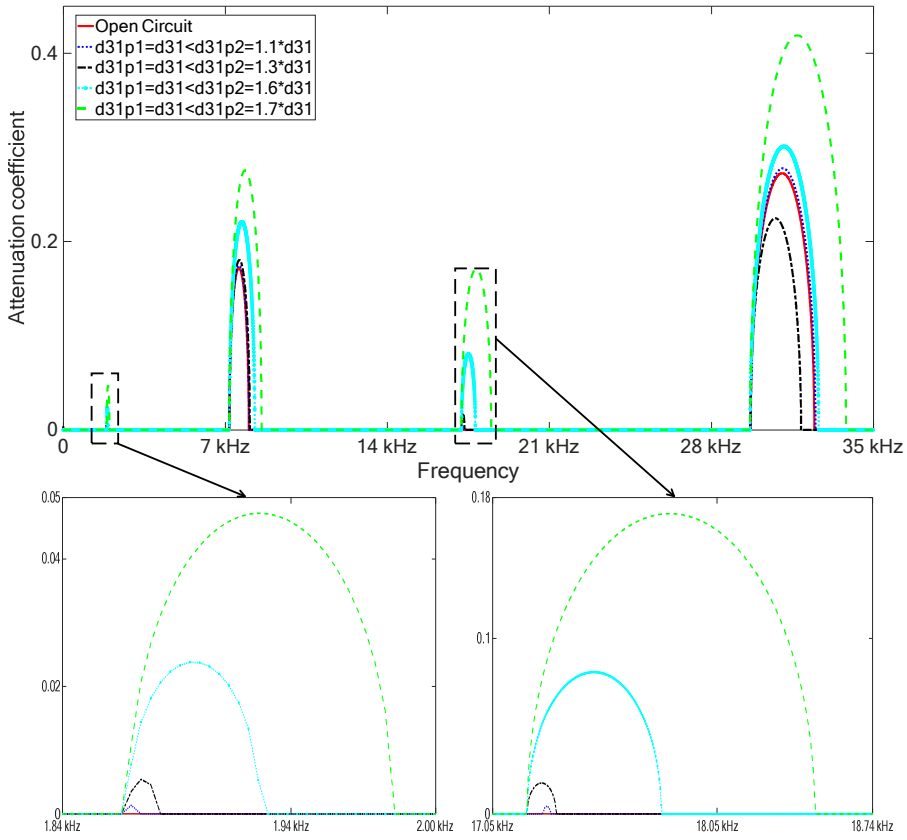
Open Circuit
d31p1=d31<d31p2=1.1*d31
d31p1=d31<d31p2=1.3*d31
d31p1=d31<d31p2=1.6*d31
d31p1=d31<d31p2=1.7*d31
Attenuation coefficient
Frequency
0
7 kHz
14 kHz
21 kHz
28 kHz
35 kHz
0.4
0.2
1.84 kHz
1.94 kHz
2.00 kHz
17.05 kHz
18.05 kHz
18.74 kHz

(a)

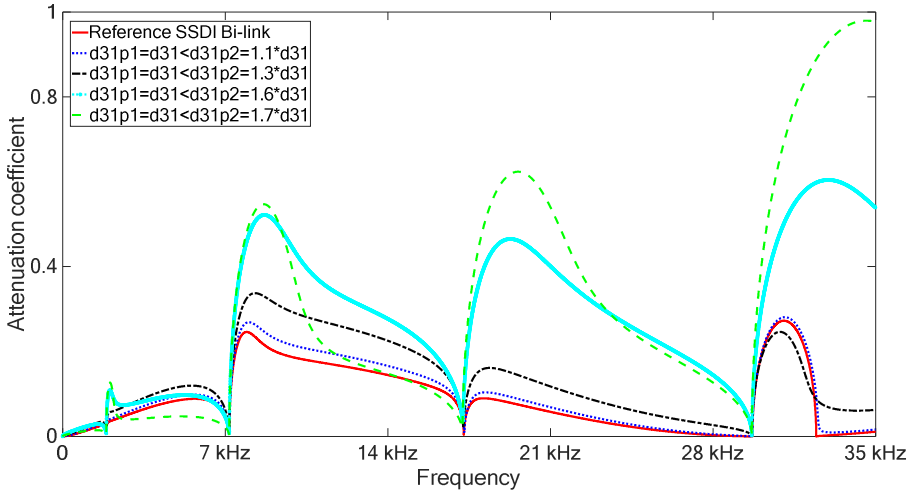
Reference SSDI Bi-link
d31p1=d31<d31p2=1.1*d31
d31p1=d31<d31p2=1.3*d31
d31p1=d31<d31p2=1.6*d31
d31p1=d31<d31p2=1.7*d31
Attenuation coefficient
Frequency
0
7 kHz
14 kHz
21 kHz
28 kHz
35 kHz
1
0.8
0.4

(b)

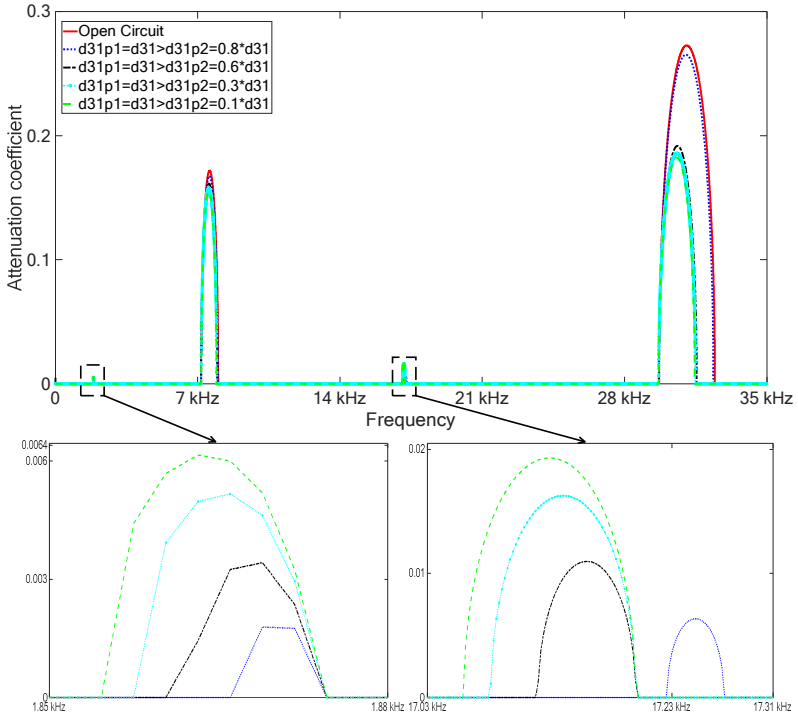

(c)

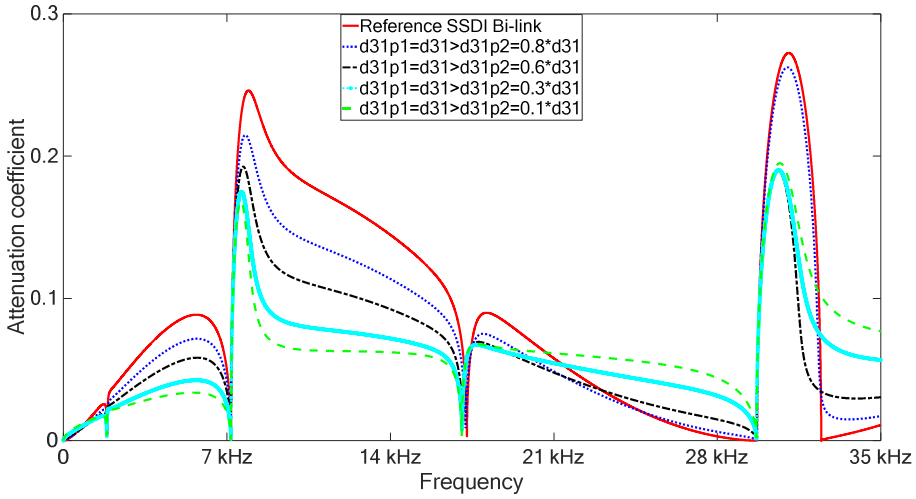

(d)

Figure 16(a) Wave attenuation performance of the investigated metamaterial in the open circuit condition with the increase of the charge coefficient of one PZT corresponding to Figure 15(a); (b) wave attenuation performance of the investigated metamaterial with the

increase of the charge coefficient of one PZT corresponding to Figure 15(a); (c) wave attenuation performance of the investigated metamaterial in the open circuit condition with the decrease of the charge coefficient of one PZT corresponding to Figure 15(b); (d) wave attenuation performance of the investigated metamaterial with the decrease of the charge coefficient of one PZT corresponding to Figure 15(b). The frequency step in the figures is 34 Hz, while the frequency step in the zoom areas of the figures is 4.2 Hz.

In the open circuit condition, the two original Bragg-type band gaps are enlarged by increasing both of charge coefficients as shown in Figure 17 (a), while being reduced with the decrease of the charge coefficients (Figure 17 (c)). For the SSDI Bi-link method, Figure 17 (b) shows that increasing both charge coefficients can improve wave attenuation performance in the whole investigated frequency range and their decrease yield reduced performance as depicted in Figure 17 (d). In addition, similar with the case when increasing the charge coefficient of one PZT, additional new Bragg-type band gaps also appear around 1.9 kHz and 17 kHz with the increase of the charge coefficients of both PZTs in the open circuit condition. Thanks to these new generated Bragg-type band gaps as shown in Figure 16(a) and Figure 17(a), the band gap hybridization coupling effects between two new generated Bragg-type band gaps and

the SSDI resonant-type band gap greatly enhance the wave attenuation performance of the investigated structure as shown in Figure 16(b) and Figure 17(b).

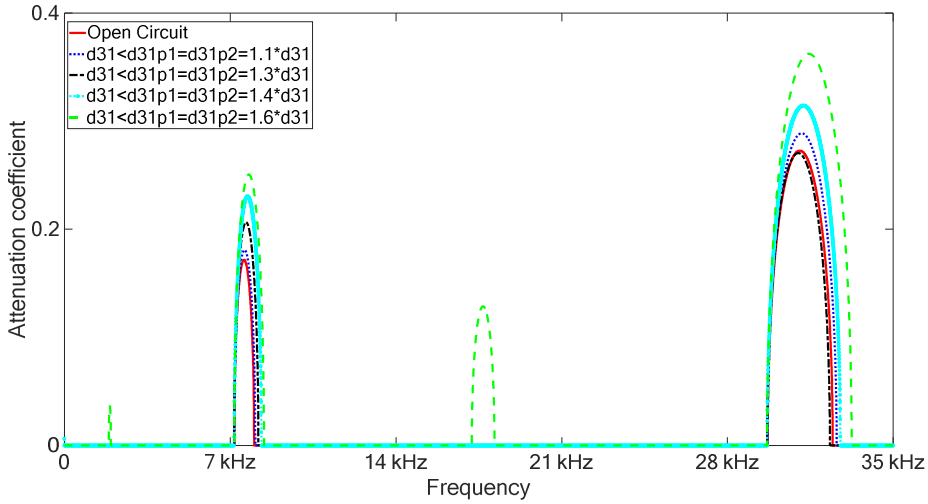

(a)

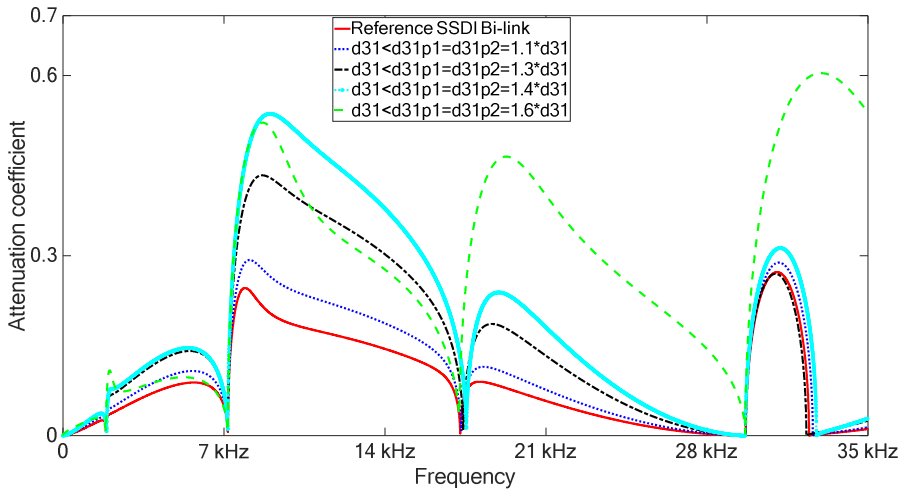

(b)

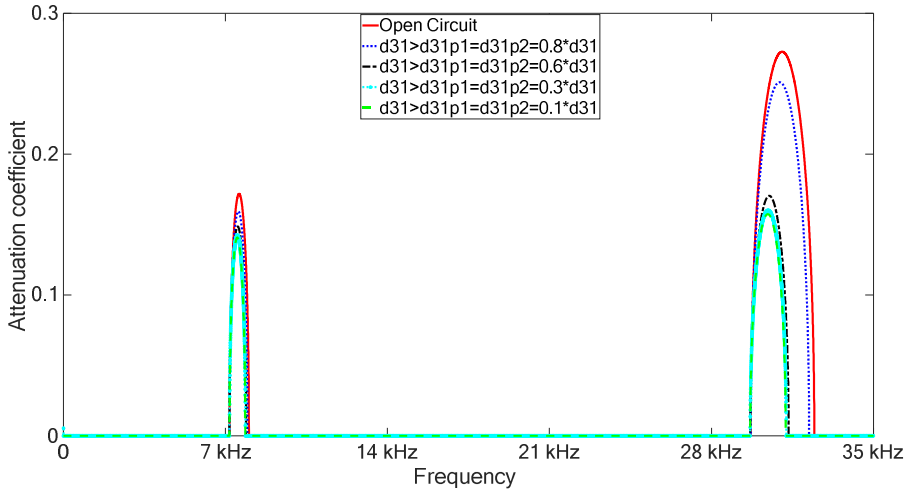

(c)

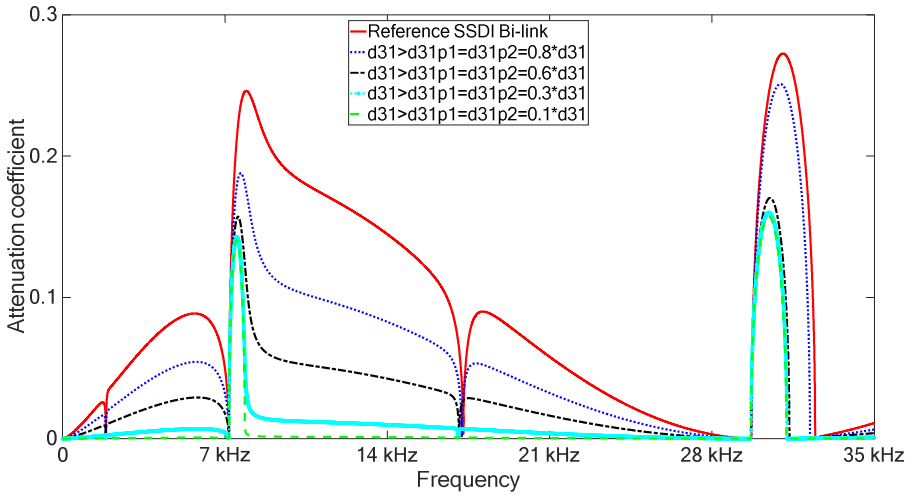

(d)

Figure 17(a) Wave attenuation performance of the investigated metamaterial in the open circuit condition with the increase of both charge coefficients corresponding to Figure 15(c); (b) wave attenuation performance of the investigated metamaterial with the increase of both charge coefficients corresponding to Figure 15(c); (c) wave attenuation performance of the investigated metamaterial in the open circuit condition with the decrease of both charge coefficients corresponding to

Figure 15(d); (d) wave attenuation performance of the investigated metamaterial with the decrease of both charge coefficients corresponding to Figure 15(d). The frequency step in the figures is 34 Hz.

4.6 Performance summary for different structural optimization methods

Table 3 and Table 4 respectively summarize wave attenuation performance of the investigated metamaterial in the open circuit condition and the SSDI Bi-link condition using the above-mentioned structural optimization methods. Four kinds of structural optimization methods including eighteen structural optimization sub-methods can be chosen according to different elastic wave manipulation requirements. Overall, for the open circuit condition as shown in Table 3, the locations of two original Bragg-type band gaps can be greatly affected by changing PZT spacing (Figure 1(b1)) and PZT lengths(Figure 1(b2)). The number of original Bragg-type band gaps within the investigated frequency domain [0 kHz, 35 kHz] can also be controlled by shifting bang gap locations (Table 3 (b1)-(b) and (d)) and sharply attenuating band gaps(Table 3(b2)-(a) and (e)). The bandwidths of the original Bragg-type band gaps can be greatly affected by changing PZT thicknesses (Figure 1(b3)) and the charge coefficients of the PZT (Figure 1(b4)). In addition,

new band gaps can also be generated by changing PZT thicknesses and the charge coefficients of the PZT. For the SSDI Bi-link method as shown in Table 4, changing the piezoelectric parameters or PZT locations in one periodic cell will globally weaken or enhance wave attenuation performance in the investigated frequency domain for most of the structural optimization methods such as (b3)-(c) and (b4)-(c). There are only a few ways to can be used to enhance specific frequency bands. For instance, wave attenuation performance in the low frequency range [0 kHz, 7.2 kHz] can be improved by the structural optimization method (b1)-(b); wave attenuation performance in the high frequency range [16.5 kHz, 35 kHz] can be improved by the structural optimization method (b3)-(e).

Open circuit	1st Bragg-type band gap [7.2 kHz, 8.1 kHz]		2nd Bragg-type band gap [29 kHz, 32 kHz]		New band gaps
	Attenuation coefficient	Location /band width	Attenuation coefficient	Location /band width	Number
(b1)-(a)	↓	←	↓	←	0
(b1)-(b)	↑	→	↑	→	0
(b1)-(c)	↓	←	↓	←	0
(b1)-(d)	↑	→	↑	→	0
(b2)-(a)	↑	→	↓	→	0

(b2)-(b)	↓	←	↓	←	1
(b2)-(c)	↑	→	↑	→	0
(b2)-(d)	↓	←	↓	←	0
(b2)-(e)	↓	→	↓	→	0
(b3)-(a)	↑	◁▷	↓	NS	2
(b3)-(b)	↓	▷◁	↓	▷◁	1
(b3)-(c)	↑	◁▷	↑	◁▷	0
(b3)-(d)	↓	▷◁	↓	▷◁	0
(b3)-(e)	↓	▷◁	↓	▷◁	2
(b4)-(a)	↑	◁▷	↑	◁▷	2
(b4)-(b)	↓	▷◁	↓	▷◁	1
(b4)-(c)	↑	◁▷	↑	◁▷	0
(b4)-(d)	↓	▷◁	↓	▷◁	0

Table 3 Summary of wave attenuation performance of the investigated metamaterial in the open circuit condition using different structural optimization methods (In the table, (b1), (b2), (b3) and (b4) respectively denote different structural optimization methods as shown in Figure 1; (a), (b), (c), (d) and (e) respectively denote the sub-methods of different optimization methods as shown in Figure 5, Figure 7, Figure 11, Figure 15. "↓" denotes that the maximal attenuation coefficient within a frequency range are gradually reduced compared with the reference case;

"↑" denotes that the maximal attenuation coefficient within a frequency range gradually goes up compared with the reference case; "↓↑" denotes that the maximal attenuation coefficient within a frequency range are firstly gradually reduced and then goes up compared with the reference case, and thus an optimal maximal attenuation coefficient exists within the frequency range; "NS" denotes that the band width of a band gap is firstly gradually reduced and then increases compared with the reference case, and thus an optimal band width exists; "→" denotes that the location of the band gap shifts to right(the higher frequency range); "←" denotes that the location of the band gap shifts to left(the lower frequency range); "◁▷" denotes that the band gap is enlarged; "▷◁" denotes that the band gap is narrowed; "---" denotes that the band gap not appears in the investigated frequency domain).

SSDI Bi-link	1st segment: [0 kHz, 1.8kHz]	2nd segment: [1.8kHz, 2 kHz]	3rd segment: [2 kHz, 7.2kHz]	4th segment: [7.2kHz, 8.1 kHz]	5th segment: [8.1 kHz, 16.5kHz]	6th segment: [16.5kHz, 29 kHz]	7th segment: [29kHz, 32kHz]	8th segment: [32kHz, 35kHz]
(b1)-(a)	↓	↓	↓	↓	↓	↑	↓	↑
(b1)-(b)	↑	↑	↑	↓	↓	↓	↓	↑
(b1)-(c)	↓	↓	↓	↓	↓	↑	↓	↑
(b1)-(d)	↑	↑	↑	↓	↓	↓	↓	↑

(b2)-(a)	↑	↑	↑	↑	↑	↑	↓	↑
(b2)-(b)	↓	↓	↓	↓	↓	↓	↓	=
(b2)-(c)	↑	↑	↑	↑	↑	NS	↓	↑
(b2)-(d)	↓	↓	↓	↓	↓	↓	↓	=
(b2)-(e)	↓	↑	↓	↓	↓	↓	↓	↑
(b3)-(a)	↑	↑	↑	↑	↑	↑	↑	↑
(b3)-(b)	↓	↓	↓	↓	↓	NS	↓	↑
(b3)-(c)	↑	↑	↑	↑	↑	↑	↑	↑
(b3)-(d)	↓	↓	↓	↓	↓	↓	↓	↑
(b3)-(e)	↓	↑	↓	↓	↓	↑	↑	↑
(b4)-(a)	↑	↑	↑	↑	↑	↑	↑	↑
(b4)-(b)	↓	↓	↓	↓	↓	↓	↓	↑
(b4)-(c)	↑	↑	↑	↑	↑	↑	↑	↑
(b4)-(d)	↓	↓	↓	↓	↓	↓	↓	↑

Table 4 Summary of wave attenuation performance of the investigated metamaterial in the SSDI Bi-link condition using different structural optimization methods (In the table, (b1), (b2), (b3) and (b4) respectively denote different structural optimization methods as shown in Figure 1; (a), (b), (c), (d) and (e) respectively denote the sub-methods of different optimization methods as shown in Figure 5, Figure 7, Figure 11, Figure 15. "↓" denotes that wave attenuation performance within a frequency

range are worse than that of the reference case; "↑" denotes that wave attenuation performance within a frequency range are better than that of the reference case; "NS" denotes that wave attenuation performance is firstly gradually weakened and then enhanced compared with the reference case, and thus optimal attenuation coefficient within the frequency range exists; "=" denotes that wave attenuation performance within a frequency range are same with the reference case).

5. Conclusion

A structural optimization work on the piezoelectric metamaterial with electrical switched Bi-link topologies based on nonlinear SSDI techniques is investigated in this article. Wave attenuation performance of the investigated structure is demonstrated theoretically based on finite element modeling method and wave propagation theory that has previously shown its ability to relate experimental investigations. From the structural optimization aspect, various factors affecting wave propagation control of the investigated metamaterial are comprehensively investigated and summarized including spacing between two PZTs in one Bi-link cell, and length / thickness / charge coefficient of two PZTs in one Bi-link cell. Results show that wave propagation characteristics of the

investigated metamaterial can be adjusted by four structural optimizing approaches including eighteen structural optimization sub-methods for meeting practical requirements as shown in Table 3 and Table 4. By virtue of the influence rules of these structural adjustments and optimizations, the investigated piezoelectric meta-structure composed of Bi-link periodic cells shows great potentials to achieve better wave attenuation manipulation performance in the desired frequency domain before fabrication.

Acknowledgments

The authors acknowledge the partial financial support from China Scholarship Council. The authors declare no conflict of interest in preparing this article.

References

[1] Bao B, Guyomar D, Lallart M, Electron–phonon metamaterial featuring nonlinear tri-interleaved piezoelectric topologies and its application in low-frequency vibration control, Smart Mater. Struct. 2016; 25(9): 095010.

[2] Chen Z, He J, Wang G, Vibration Bandgaps of Piezoelectric Metamaterial Plate with Local Resonators for Vibration Energy Harvesting, Shock Vib. 2019; Article ID 1397123.

[3] Pan W, Tang G, Tang J, Evaluation of uncertainty effects to band gap behavior of circuitry-integrated piezoelectric metamaterial using order-reduced analysis. J. Intell. Mater. Syst. Struct., 2018; 29(12): 2677–2692.

[4] Sugino C, Ruzzene M, Erturk A, Design and Analysis of Piezoelectric Metamaterial Beams With Synthetic Impedance Shunt Circuits. IEEE/ASME T Mech, 2018; 23(5): 2144-2155.

[5] Sugino C, Ruzzene M, Erturk A, Merging mechanical and electromechanical bandgaps in locally resonant metamaterials and metastructures. J Mech Phys Solids, 2018; 116: 323-333.

[6] Newnham R, Ruschau G R, Electromechanical properties of smart materials. J. Intell. Mater. Syst. Struct., 1993; 4(3): 289-294.

[7] Liu Z, Zhang X, Mao Y, et al. Locally resonant sonic materials. Science, 2000; 289(5485): 1734-1736.

[8] Jin Y, Bonello B, Pan Y, Acoustic metamaterials with piezoelectric resonant structures. J Phys D Appl Phys, 2014; 47(24): 245301.

[9] Bao B, Guyomar D, Lallart M, Vibration reduction for smart periodic structures via periodic piezoelectric arrays with nonlinear interleaved-switched electronic networks, Mech. Syst. Sig. Process. 2017; 82: 230-259.

[10] Han J, Tang S, Realization of complex curved waveguide based on local resonant 3D metamaterial. AIP Adv, 2018; 8: 125327.

[11] Lee J H, Singer J P, Thomas E L, Micro-/Nanostructured Mechanical Metamaterials. Adv mater, 2012; 24(36): 4782-4810.

[12] Lu K , Wu J H , Jing L , et al. The two-degree-of-freedom local resonance elastic metamaterial plate with broadband low-frequency bandgaps. J Phys D Appl Phys, 2017; 50(9):095104.

[13] Xu X, Barnhart M, Li X, et al. Tailoring Vibration Suppression Bands with Hierarchical Metamaterials Containing Local Resonators. J Sound Vib. 2018; 442: 10.1016/j.jsv.2018.10.065.

[14] Fomenko S I, Golub M V, Chen A, Wang Y S, Zhang C Z, Band-gap and pass-band classification for oblique waves propagating in a three-dimensional layered functionally graded piezoelectric phononic crystal, J Sound Vib. 2019; 439: 219-240.

[15] Kherraz N , F.-H C B, R Sainidou, et al. Tunable phononic structures using Lamb waves in a piezoceramic plate. Phys Rev B. 2019; 99.094302.

[16] Zhou W J, Wu B, Muhammad Du, et al. Actively tunable transverse waves in soft membrane-type acoustic metamaterials. J Appl Phys, 2018; 123, 165304.

[17] Tateo F, Collet M, Ouisse M, et al. Design variables for optimizing adaptive metacomposite made of shunted piezoelectric patches distribution. J Vib Control, 2014: 1077546314545100.

[18] Bergamini A, Delpero T, Simoni L D, et al. Phononic Crystal with Adaptive Connectivity. Adv Mater, 2014; 26(9): 1343-1347.

[19] Chen S, Wang G, Wen J, et al. Wave propagation and attenuation in plates with periodic arrays of shunted piezo-patches. J Sound Vib, 2013; 332(6): 1520-1532.
[20] Xu J W, Yan R Q, Tang J T. Broadening Bandgap Width of Piezoelectric Metamaterial by Introducing Cavity. Appl Sci. 2018; 8(9):10.3390/app8091606.
[21] Maurini C, Dell'Isola F, Vescovo D D, Comparison of piezoelectronic networks acting as distributed vibration absorbers. Mech. Syst. Sig. Process, 2004; 18(5): 1243-1271.
[22] Kherraz N, Haumesser L, Levassort F, et al. Hybridization bandgap induced by an electrical resonance in piezoelectric metamaterial plates. J Appl Phys, 2018; 123(9): 094901.
[23] Lee J, Daniel S B, Optimal shunt parameters for maximising wave attenuation with periodic piezoelectric patches. J. Intell. Mater. Syst. Struct., 2016; 28(1): 108-123.
[24] Xu J, Yan R, Exploitation of dimension-dependent behavior of piezoelectric metamaterial with LC shunt circuit. Eur. Phys. J. Appl. Phys., 2018; 83(2): DOI: 10.1051/epjap/2018180124.
[25] Tang W, Wang B, Bao B, et al, Experimental Comparisons of two detection methods for semi-passive piezoelectric structural damping. J vib eng technol, 2017, 5(4): 367-379.
[26] Beck B S, Cunefare K A, Ruzzene M, et al. Experimental Analysis of a Cantilever Beam with a Shunted Piezoelectric Periodic Array. J. Intell. Mater. Syst. Struct., 2010, 22(22):1177-1187.
[27] Chen, Y Y, Zhu R, Barnhart M V, et al, Enhanced flexural wave sensing by adaptive gradient-index metamaterials. Sci Rep, 2016. 6: 35048.
[28] Ning L, Wang Y Z, Wang Y S. Active control of a black hole or concentrator for flexural waves in an elastic metamaterial plate. Mech Mater, 2020, 142:103300.
[29] Chen P, Wang Y Z, Wang Y S. Active control of flexural waves in a phononic crystal beam with staggered periodic properties. Wave Motion,2020, 93: 102481.
[30] Bao B, Wang Q. Elastic wave manipulation in piezoelectric beam meta-structure using electronic negative capacitance dual-adjacent/staggered connections. Compos. Struct., 2019, 210: 567-580.
[31] Chen Y Y, Huang G L, Sun C T. Band gap control in an active elastic metamaterial with negative capacitance piezoelectric shunting. J Vib Acoust, 2014. 136(6): 061008.
[32] Li X P, Chen Y Y, Hu G K, et al, A self-adaptive metamaterial beam with digitally controlled resonators for subwavelength broadband flexural wave attenuation. Smart Mater. Struct., 2018. 27(4): 045015.
[33] Sang S, Mhannawee A, Wang Z, A design of active elastic metamaterials with negative mass density and tunable bulk modulus. Acta Mech, 2019. 230(3): 1003-1008.
[34] Wang Y, Niu S, Hu Y, A periodic piezoelectric smart structure with the integrated passive/active vibration-reduction performances. Smart Mater. Struct., 2017. 26(6): 065015.

[35] Chen Y, Hu G, Huang G, A hybrid elastic metamaterial with negative mass density and tunable bending stiffness. J Mech Phys Solids, 2017; 105: 179-198.
[36] Fan Y, Collet M, Ichchou M, et al., A wave-based design of semi-active piezoelectric composites for broadband vibration control. Smart Mater. Struct., 2016. 25(5): 055032.
[37] Yi, K., Ouisse M, Sadoulet-Reboul E, et al, Active metamaterials with broadband controllable stiffness for tunable band gaps and non-reciprocal wave propagation. Smart Mater. Struct., 2019; 28(6): 065025.
[38] Bao B, Guyomar D, Lallart M, Piezoelectric metacomposite structure carrying nonlinear multilevel interleaved-interconnected switched electronic networks, Compos. Struct. 2017; 161: 308-329.
[39] Yan L-J, Bao B, Guyomar D, Lallart M, Periodic structure with interconnected nonlinear electrical networks, J. Intell. Mater. Syst. Struct. 2016; 1045389X16649448.
[40] Liang B, Guo X S, Tu J, et al, An acoustic rectifier. Nature Materials, 2010; 9: 989-992.
[41] Bilal O R, Foehr A, Daraio C, Reprogrammable Phononic Metasurfaces. Adv Mater, 2017; 29(39): 1700628.
[42] Bilal O R, Foehr A, Daraio C, Bistable metamaterial for switching and cascading elastic vibrations. P Natl A Sci, 2017; 114(18): 4603-4606.
[43] Lallart M, Yan L, Richard C, Guyomar D, Damping of periodic bending structures featuring nonlinearly interfaced piezoelectric elements, J. Vib. Control. 2015; 22(18):3930-3941.
[44] Lallart M, Lefeuvre E, Richard C, Guyomar D, Self-Powered Circuit for Broadband, Multimodal Piezoelectric Vibration Control, Sens. Act. A: Phys. 2008, 143(2): 277-382.
[45] Zheng Y, Wu Z, Zhang X, et al., A piezo-metastructure with bistable circuit shunts for adaptive nonreciprocal wave transmission. Smart Mater. Struct, 2018. 28(4): 045005.
[46] Harne R L, Wang K W, Robust sensing methodology for detecting change with bistable circuitry dynamics tailoring. Appl Phys Lett, 2013. 102(20): 203506.
[47] Bao B, Lallart M, Guyomar D. Manipulating elastic waves through piezoelectric metamaterial with nonlinear electrical switched Dual-connected topologies. Int J Mech Sci, 2020: 105423.
[48] Wu Y, Li L, Fan Y, et al. A linearised analysis for structures with synchronized switch damping. IEEE Access, 2019, 7: 133668-133685.
[49] Zhang F, Li L, Fan Y, et al. Dual-connected Synchronized Switch Damping for Vibration Control of Bladed Disks in Aero-engines. Appl Sci, 2020, 10(4): 1478.
[50] Chen A L, Wang Y S, Zhang C Z. Wave propagation in one-dimensional solid-fluid quasi-periodic and aperiodic phononiccrystals. Physica B: Condens. Matter, 2012, 407: 324–329.

Graphical Abstract: